

**This is a self-archived version of an original article. This version may differ from the original in pagination and typographic details.**

**Author(s):** Dods, Robert; Båth, Petra; Morozov, Dmitry; Gagnér, Viktor Ahlberg; Arnlund, David; Luk, Hoi Ling; Kübel, Joachim; Maj, Michat; Vallejos, Adams; Wickstrand, Cecilia; Bosman, Robert; Beyerlein, Kenneth R.; Nelson, Garrett; Liang, Mengning; Milathianaki, Despina; Robinson, Joseph; Harimoorthy, Rajiv; Berntsen, Peter; Malmerberg, Erik; Johansson, Linda; Andersson, Rebecka; Carbajo, Sergio;

**Title:** Ultrafast structural changes within a photosynthetic reaction centre

**Year:** 2021

**Version:** Accepted version (Final draft)

**Copyright:** © Nature Publishing Group, 2020

**Rights:** In Copyright

**Rights url:** <http://rightsstatements.org/page/InC/1.0/?language=en>

**Please cite the original version:**

Dods, R., Båth, P., Morozov, D., Gagnér, V. A., Arnlund, D., Luk, H. L., Kübel, J., Maj, M., Vallejos, A., Wickstrand, C., Bosman, R., Beyerlein, K. R., Nelson, G., Liang, M., Milathianaki, D., Robinson, J., Harimoorthy, R., Berntsen, P., Malmerberg, E., . . . Neutze, R. (2021). Ultrafast structural changes within a photosynthetic reaction centre. *Nature*, 589(7841), 310-314.  
<https://doi.org/10.1038/s41586-020-3000-7>



25 <sup>7</sup>*Australian Research Council Centre of Excellence in Advanced Molecular Imaging, La*  
26 *Trobe Institute for Molecular Science, La Trobe University, Melbourne 3086, Australia*

27 <sup>8</sup>*Molecular Biophysics and Integrated Bioimaging, Lawrence Berkeley National Laboratory,*  
28 *Berkeley, CA, USA.*

29 <sup>9</sup>*The Bridge Institute, Department of Chemistry, University of Southern California, Los*  
30 *Angeles, CA 90089-3303, USA.*

31 <sup>10</sup>*Institut de Biologie Structurale (IBS), Université Grenoble Alpes, CEA, CNRS, F-38000*  
32 *Grenoble, France*

33 <sup>11</sup>*European Synchrotron Radiation Facility, F-38043 Grenoble, France.*

34 <sup>12</sup>*Department of Chemistry-Ångström laboratory, Uppsala University, Uppsala, Sweden.*

35

36

37

38

39 †These authors contributed equally to this work.

40 \*Corresponding author: [richard.neutze@gu.se](mailto:richard.neutze@gu.se)

41

42 **Photosynthetic reaction centres harvest the energy content of sunlight by transporting**  
43 **electrons across an energy transducing biological membrane. We use time-resolved**  
44 **serial femtosecond crystallography<sup>1</sup> at an X-ray free electron laser<sup>2</sup> to observe light-**  
45 **induced structural changes in the photosynthetic reaction centre of *Blastochloris viridis***  
46 **on a time-scale of picoseconds. Structural perturbations are first centred upon the**  
47 **protein's special pair of chlorophyll molecules that are photo-oxidized by light. Electron**  
48 **transfer to the menaquinone acceptor on the opposite side of the membrane induces a**  
49 **movement of this cofactor in concert with lower amplitude protein rearrangements.**  
50 **These observations reveal how proteins utilize conformational dynamics to stabilize the**  
51 **charge separation steps of electron transfer reactions.**

52

53 Our biosphere depends upon the electron transfer reactions of photosynthesis as a primary  
54 source of energy. Photosystems and photosynthetic reaction centres form a family of integral  
55 membrane protein complexes found in plants, algae, cyanobacteria and photosynthetic  
56 bacteria that convert the energy of a captured photon into a charge separated state. The  
57 photosynthetic reaction centre of the purple non-sulphur bacterium *Blastochloris viridis*  
58 ( $RC_{vir}$ ) contains three transmembrane subunits called H, L and M and a periplasmic subunit C.  
59 These subunits support four bacteriochlorophyll molecules (BCh), two bacteriopheophytin  
60 molecules (BPh), a tightly bound menaquinone ( $Q_A$ ), a mobile ubiquinone ( $Q_B$ ), a single non-  
61 haem iron and four haem co-factors (**Fig. 1**). Electron transfer reactions originate at a special  
62 pair (SP) of strongly interacting bacteriochlorophylls which in *Bl. viridis* have an absorption  
63 maximum at 960 nm. Photo-oxidation of the SP liberates an electron which is transferred to  
64 the active branch  $BPh_L$  within a few picoseconds, is transferred to the tightly bound  
65 menaquinone ( $Q_A$ ) in less than a nanosecond, and is transferred to the mobile ubiquinone ( $Q_B$ )  
66 in microseconds.  $SP^+$  is reduced by subunit C and a second photo-oxidation event transfers a

67 second electron to  $Q_B^-$ , which is protonated from the cytoplasm and released into the  
68 membrane as ubiquinol ( $H_2Q$ ). Other proteins participate in a cyclic flow that returns  
69 electrons to subunit C and the net effect is that two protons are transported across an energy-  
70 transducing membrane for every photon absorbed.

71

72 Electrons may tunnel between cofactors when they are separated by approximately 10 Å or  
73 less.<sup>3</sup> The primary electron transfer step from SP to  $BPh_L$  occurs in  $2.8 \pm 0.2$  ps<sup>4</sup> over a  
74 distance of 10 Å by means of a two-step hopping mechanism *via* the monomeric  $BCh_L$ <sup>5</sup> and is  
75 more rapid than conventional Marcus theory. By contrast, the 9 Å electron transfer step from  
76  $BPh_L$  to  $Q_A$  has a single exponential decay time of  $230 \pm 30$  ps<sup>6</sup> which is consistent with  
77 conventional Marcus theory. Coherent nuclear motions<sup>7</sup> and protein structural changes<sup>8</sup> have  
78 been suggested to influence the initial charge-transfer reactions of photosynthesis yet the  
79 specific nature of these putative protein motions is unknown. Flash-freeze crystallographic  
80 trapping studies,<sup>9</sup> time-resolved Laue diffraction<sup>10</sup> and time-resolved serial femtosecond  
81 crystallography<sup>11-14</sup> (TR-SFX) have revealed structural changes in bacterial photosynthetic  
82 reaction centres<sup>9,10</sup> and cyanobacterial photosystem II<sup>11-14</sup> that occur on the late microsecond  
83 to millisecond time-scale, yet no time-resolved crystallographic studies on the time-scale of  
84 the primary charge separation reactions of photosynthesis have been reported.

85

86 Here we apply time-resolved serial femtosecond crystallography<sup>1</sup> at an X-ray free electron  
87 laser (XFEL) to probe the ultrafast structural response of  $RC_{vir}$  to light. We photo-excited the  
88 special pair with 150 fs pulses centred at 960 nm (Extended Data Fig. 1). X-ray pulses 40 fs in  
89 duration were generated at the LCLS<sup>2</sup> and were used to record diffraction patterns from tens  
90 of thousands of microcrystals for the time points  $\Delta t = 1$  ps, 5 ps (two repeats), 20 ps, 300 ps  
91 (two repeats) and 8  $\mu$ s after photoexcitation (Extended Data Table 1). The time point  $\Delta t = 1$  ps

92 populates the photo-excited charge transfer state of the SP in which charge rearrangements  
93 have occurred within the bacteriochlorophyll dimer but are prior to the primary electron  
94 transfer step;  $\Delta t = 5$  and 20 ps are after the initial charge-transfer step and SP is oxidized and  
95 BPh<sub>L</sub> is reduced;  $\Delta t = 300$  ps is longer than the time constant for electron transfer to Q<sub>A</sub> and  
96 menaquinone is reduced; and  $\Delta t = 8 \mu\text{s}$  corresponds to a meta-stable charge separated state.

97

98 Extended Data Fig. 2 presents overviews of the  $|F_{\text{obs}}|^{\text{light}} - |F_{\text{obs}}|^{\text{dark}}$  isomorphous difference  
99 Fourier electron density maps (“light” corresponds to data collected from photo-activated  
100 microcrystals whereas “dark” corresponds to data collected from microcrystals that were not  
101 photo-activated) for all time points. Difference electron density features are visible above 4.0  
102  $\sigma$  ( $\sigma$  is the root mean square electron density of the map) near SP for all time points and  
103 strong features associated with Q<sub>A</sub> are visible for  $\Delta t \geq 300$  ps (Extended Data Table 2). In  
104 contradistinction with ultrafast TR-SFX studies of bacteriorhodopsin,<sup>15</sup> photoactive yellow  
105 protein,<sup>16</sup> rsEGFP<sup>17</sup> and bacterial phytochromes<sup>18</sup> in which ultrafast structural changes are  
106 driven by the movements of atoms due to a photo-isomerization event, TR-SFX  
107 measurements of RC<sub>vir</sub> reveal a knock-on effect on protein structure due to the light-induced  
108 redistribution of charge. Electric-field induced conformational changes have been observed  
109 when fields of the order  $10^8$  V/m are applied across a protein-crystal<sup>19</sup> and this is the same  
110 order of magnitude as electric field perturbations due to the movement of an electron within  
111 RC<sub>vir</sub>.

112

113 Recurring changes of electron density are visible as positive difference electron density in the  
114 region of overlap between the two bacteriochlorophylls SP<sub>L</sub> and SP<sub>M</sub> of the special pair, and  
115 complementary negative difference electron density features are visible primarily associated  
116 with SP<sub>M</sub> (Fig. 2, Extended Data Fig. 3, Extended Data Table 2, Supplementary Video 1).

117 Singular value decomposition (SVD) of all seven difference Fourier electron density maps  
118 (Fig. 2e) reveals that the strongest positive and several of the strongest negative difference  
119 electron density features of the principal SVD component are associated with the SP  
120 (Extended Data Table 2). Quantification of electron density changes<sup>20</sup> within the RC<sub>vir</sub> co-  
121 factors (Fig. 2f) and statistical tests against control difference Fourier electron density maps  
122 (Methods) provides a very high-level of confidence ( $p$ -value  $\leq 0.001$ , Extended data Table 3)  
123 that these recurring difference electron density features do not arise by chance. Thus  
124 photoexcitation causes the bacteriochlorophylls of SP to move closer together and the bending  
125 (an out of plane distortion) of SP<sub>M</sub> could explain these observations. An out of plane  
126 distortion was used to model difference electron density features observed as carbon  
127 monoxide was photo-dissociated from the haem of myoglobin<sup>21</sup> (Extended Data Fig. 4).  
128 Nonplanar distortions of chlorin and bacteriochlorin rings are observed in photosystem II and  
129 RC<sub>sph</sub> due to interactions with the surrounding protein<sup>22</sup> and nonplanar porphyrins are also  
130 more easily oxidized than planar porphyrins.<sup>23,24</sup> This suggests that the distortion of SP in  
131 advance of the primary charge separation event (Fig. 2a) could enhance the yield of the  
132 primary charge-transfer reaction, which has been optimized by evolution to achieve almost  
133 perfect quantum efficiency.<sup>25</sup>

134

135 When the C-subunit is fully reduced, an electron is transferred from haem<sub>3</sub> to SP<sup>+</sup> in less than  
136 a microsecond.<sup>26</sup> The above reasoning implies that SP<sup>+</sup> may be more easily reduced should  
137 SP<sub>M</sub> return to a planar geometry before this electron transfer occurs. This hypothesis is  
138 consistent with our experimental observations since the amplitude of the positive difference  
139 electron density feature between the SP bacteriochlorophylls increases from  $\Delta t = 1$  ps to 20  
140 ps, decreases for  $\Delta t = 300$  ps and is insignificant for  $\Delta t = 8$   $\mu$ s (Fig. 2, Extended Data Fig. 3,  
141 Extended Data Table 2). Moreover, neither TR-SFX studies of the S2→S3 transition of

142 cyanobacteria PSII<sup>13</sup> ( $\Delta t = 150 \mu\text{s}$  and  $400 \mu\text{s}$ ) nor TR-Laue diffraction studies of RC<sub>vir</sub><sup>10</sup> ( $\Delta t =$   
143  $3 \text{ ms}$ ) report a positive difference electron density feature in the region of overlap between the  
144 special pair of (bacterio)chlorophylls, implying that this feature has decayed.

145

146 Charge rearrangements cause SP<sup>+</sup> to move up to  $0.3 \text{ \AA}$  towards the M-subunit by  $\Delta t = 300 \text{ ps}$   
147 and the side-chains of both His173<sub>L</sub> and His200<sub>M</sub> adjust to preserve their ligating interactions  
148 with the magnesium ions of SP<sup>+</sup>, as do His168<sub>L</sub> and Tyr195<sub>M</sub> adjust conformation in order to  
149 maintain their H-bond interactions to SP<sub>L</sub> and SP<sub>M</sub> respectively. These structural perturbations  
150 are revealed by paired negative and positive difference electron density features on the side-  
151 chain of His173<sub>L</sub> in the principal SVD components calculated from both the early (1ps,  $2 \times$   
152  $5 \text{ ps}$ ,  $20 \text{ ps}$ ) and late ( $2 \times 300 \text{ ps}$ ,  $8 \mu\text{s}$ ) sub-sets of TR-SFX data, whereas positive difference  
153 electron density features associated with the side-chains of His200<sub>M</sub> and Tyr195<sub>M</sub> become  
154 noticeably stronger for the later sub-set of data (Extended Data Fig. 3i,j; Extended Data Table  
155 2; Supplementary Video 1). These observations suggest that SP<sub>L</sub> moves towards subunit M  
156 slightly in advance of SP<sub>M</sub>, which may be due to dielectric asymmetry within photosynthetic  
157 reaction centres.<sup>27,28</sup> Dielectric asymmetry is believed to underpin the phenomenon that  
158 electron transfer occurs only along the A-branch<sup>27</sup> in purple bacteria RCs and PSII (Fig. 1).

159

160 An electron moves from SP to BPh<sub>L</sub> in  $2.8 \pm 0.2 \text{ ps}^4$  and from BPh<sub>L</sub> to Q<sub>A</sub> in  $230 \pm 30 \text{ ps}^6$   
161 The tightly bound menaquinone is therefore neutral for  $\Delta t = 1 \text{ ps}$ ,  $5 \text{ ps}$  and  $20 \text{ ps}$ ; three-  
162 quarters of the photo-activated population are reduced to semiquinone by  $\Delta t = 300 \text{ ps}$ ; and  
163 essentially all photo-activated molecules have Q<sub>A</sub> reduced at  $\Delta t = 8 \mu\text{s}$ . Our difference  
164 Fourier electron density maps confirm these expectations since the few difference electron  
165 density features visible within the Q<sub>A</sub> binding pocket for  $\Delta t \leq 20 \text{ ps}$  are isolated whereas more  
166 continuous paired positive and negative difference electron density features are visible for  $\Delta t$

167  $\geq 300$  ps (Fig. 3, Extended Data Fig. 5). These recurring features of the later sub-set of TR-  
168 SFX data ( $2 \times 300$  ps,  $8 \mu\text{s}$ ) produce strong difference electron density features in the  
169 principal SVD component that are associated with  $Q_A$  and its H-bond interaction with  
170 His217<sub>M</sub> (Extended Data Table 2, Fig. 3d, Supplementary Video 2) and statistical tests  
171 establish that these recurring changes cannot be ascribed to noise ( $p\text{-value} \leq 0.0125$ , Extended  
172 Data Table 3). Structural refinement models these observations as due to a twist and  
173 translation of the semiquinone that brings the negatively charged head-group approximately  
174  $0.2 \text{ \AA}$  closer to the positive charge of the non-haem  $\text{Fe}^{2+}$  (Fig. 3f) and thereby stabilizes the  
175 reduced form of this cofactor. This interpretation receives support from QM/MM calculations  
176 that predict that the  $Q_A$  to His217<sub>M</sub> H-bond is shortened by  $0.17 \text{ \AA}$  when  $Q_A$  is reduced  
177 (Extended Data Fig. 6f) and suggest that semiquinone binding is stabilized by approximately  
178  $36 \text{ kJ.mol}^{-1}$  due to structural changes (Extended Data Fig. 6g,h, Methods), which is a sizeable  
179 fraction of the energy ( $125 \text{ kJ.mol}^{-1}$ ) of a  $960 \text{ nm}$  photon. Similar conclusions were drawn  
180 from an earlier analysis using a Density Functional Theory (DFT) formalism.<sup>29</sup> Light-induced  
181 electron density changes were visible for  $Q_A$  in TR-SFX studies of the S2→S3 transition of  
182 cyanobacteria PSII<sup>13</sup> for the time points  $150 \mu\text{s}$  and  $400 \mu\text{s}$ , light-induced movements of the  
183 mobile quinone  $Q_B$  were also observed in PSII<sup>11-14</sup> for delays of hundreds of milliseconds, and  
184 larger light-induced motions of  $Q_B$  were reported in freeze-trapping studies of the  
185 *Rhodobacter sphaeroides* photosynthetic reaction centre.<sup>9</sup>

186

187 For  $\Delta t = 300$  ps, paired negative and positive difference electron density features are  
188 associated with the cytoplasmic portions of TM helices  $D_M$  and  $E_M$  (Fig. 3e) and indicate that  
189  $\text{RC}_{vir}$  adjusts its structure in response to the movement of the semiquinone within the  $Q_A$   
190 binding pocket (Fig. 3f). A more quantitative analysis (Methods, Extended Data Fig. 7,  
191 Supplementary Video 3) suggests that low-amplitude protein motions begin to arise already

192 by  $\Delta t = 1$  ps (Fig. 4a) as observed in TR-SFX studies of bR<sup>15,20</sup> and Mb:CO<sup>21</sup>; the amplitude  
193 of these motions increase with time and by  $\Delta t = 5$  ps larger displacements are observed near  
194 the SP<sup>+</sup> and BPh<sub>L</sub><sup>-</sup> cofactors (Fig. 4b); and for  $\Delta t = 300$  ps protein conformational changes  
195 extend throughout the A-branch of the electron transfer pathway from SP<sup>+</sup> to Q<sub>A</sub><sup>-</sup> (Fig. 4c).  
196 When the same representation is used to depict protein conformational changes predicted  
197 from QM/MM calculations (Supplementary Video 4) almost no structural changes are  
198 expected for the photo-excited charge transfer state (Fig. 4d); protein movements arise near  
199 the charged cofactors in the SP<sup>+</sup>:BPh<sub>L</sub><sup>-</sup> charge-separated state (Fig. 4e); and structural changes  
200 extend throughout the A-branch in the SP<sup>+</sup>:Q<sub>A</sub><sup>-</sup> charge-separated state (Fig. 4f). These  
201 findings demonstrate that RC<sub>vir</sub> is not a passive scaffold but rather low-amplitude protein  
202 motions engage in a choreographed dance with electron movements taking the lead and  
203 protein conformational changes following. Conversely, as the protein's structure adjusts to  
204 stabilize these charge rearrangements the energetic barriers hindering the reverse electron  
205 transfer reaction increase, thereby extending the lifetime of the charge separated species and  
206 enhancing the overall efficiency of photosynthesis.

207

208 In Marcus theory the total potential energy of an electron donor and its surroundings must be  
209 equal to that of the electron acceptor and its surroundings if an electron is to tunnel from  
210 donor to acceptor.<sup>3</sup> Fluctuations in the organizational energy around protein cofactors are  
211 therefore essential to facilitate electron transfer reactions. Efforts aimed at understanding how  
212 protein conformational dynamics control the rates of electron transfer between cofactors<sup>8,30</sup>  
213 have been hampered by a lack of experimental tools that characterize protein structural  
214 changes on the relevant time-scales. Our observations provide an experimental framework for  
215 extending the standard description of electron transfer reactions in photosynthesis<sup>3</sup> to  
216 explicitly incorporate protein structural changes. Electron transfer reactions are ubiquitous in

217 nature and therefore a more nuanced understanding of the interplay between protein structural  
218 dynamics and the movement of electrons has far-reaching biochemical significance.

219

220

221 **Extended Data** is available for this manuscript.

222

223 **Supplementary Information** is available for this manuscript.

224

225 **Acknowledgements** Use of the Linac Coherent Light Source (LCLS), SLAC National  
226 Accelerator Laboratory, is supported by the U.S. Department of Energy, Office of Science,  
227 Office of Basic Energy Sciences under Contract No. DE-AC02-76SF00515. Parts of the  
228 sample delivery system used at LCLS for this research was funded by the NIH grant  
229 P41GM103393, formerly P41RR001209. Complementary studies were performed at BL3 of  
230 SACLA with the approval of the Japan Synchrotron Radiation Research Institute (JASRI,  
231 proposal number 2018B8068). RN acknowledges funding from the European Commission  
232 Marie Curie Training Networks (X-Probe, NanoMem), the European Union's Horizon 2020  
233 research and innovation programme (grant agreement No. 789030) and the Swedish Research  
234 Council (grant No. 2015-00560 and 349-2011-6485), the Swedish Foundation for Strategic  
235 Research (grant SRL10-0036), and the Knut and Alice Wallenberg Foundation (grant KAW  
236 2012.0284, KAW 2012.0275 and KAW 2014.0275). GB acknowledges funding from the  
237 Swedish Research Council (grant 2017-06734) and the Swedish Foundation for Strategic  
238 Research (grant ID17-0060). GG and HLL acknowledge funding from the Academy of  
239 Finland (grants 290677 and 304455), the BioExcel CoE project funded by the European  
240 Union contracts H2020-INFRAEDI-02-2018-823830 and H2020-EINFRA-2015-1-675728,  
241 and the CSC-IT centre in Espoo for access to computing resources. R.N. wishes to thank  
242 Professors Neal Woodbury for discussions.

243

244 **Author Information**

245 These authors contributed equally: Robert Dods, Petra Båth.

246

247 **Contributions**

248 R.N. conceived the experiment, which was designed with input from G.B., R.D., J.D., S.B.,  
249 M.L., S.C., D.M., M.S.H., G.J.W., J.D., D.P.D. and A.B. Samples were prepared by R.D.,  
250 P.Bå., D.A. and R.B. Crystallization was supervised by G.B.. Time-resolved serial  
251 femtosecond crystallography experiments were performed at the LCLS by R.D., P.Bå., D.A.,  
252 R.B. K.R.B., G.N., M.L., D.M., J.R., R.H., P.Be., E.M., L.J., R.A., S.C., E.C., C.E.C., P.D.,  
253 G.H., M.S.H., C.L., S.L. C.S., A.S., G.J.W., C.W., J.D., D.P.D., A.B., G.B. and R.N. The CXI  
254 instrument was set up and run by M.L., M.S.H., G.J.W. and S.B.. The photoexcitation laser of  
255 960 nm was operated and aligned by D.M., J.R., S.C. and J.D.. Sample delivery was  
256 performed by K.R.B., G.N., R.H., P.Be., P.D. and D.P.D. Data were analysed by R.D., P.Bå.,  
257 A.R., O.Y., A.B., G.B. and R.N. Structural refinement was performed by R.D. and P.Bå.  
258 Resampling, full occupancy structural refinement and analysis were performed by V.A.G,  
259 G.K. and A.V. Integration within a sphere and statistical tests were performed by C.W., R.N.  
260 and P.Bå.. SVD analysis was performed by A.V. Quantum Mechanics/Molecular Mechanics  
261 analysis were performed by D.M., H.L.L and G.G.. Time-resolved IR spectroscopy  
262 measurements were performed by J.K, M.M and S.W. The manuscript was prepared by R.N.,  
263 P.Bå., R.D. and G.B. with additional input from all authors.

264

265 **Corresponding Author**

266 Correspondence to Richard Neutze (richard.neutze@gu.se).

267

268 **Code Availability**

269 Software used for SVD analysis is available at <https://github.com/Neutze-lab/SVD>. Code  
270 written in MATLAB to analyse difference electron density amplitudes is available at

271 <https://github.com/Neutze-lab/maptool>. Software associated with the resampling of X-ray  
272 diffraction data is available at [https://github.com/Katona-lab/CFEL\\_tools](https://github.com/Katona-lab/CFEL_tools).

273

#### 274 **Data Availability**

275 Atomic coordinates and structure factors have been deposited in the Protein Data Bank,  
276 [www.pdb.org](http://www.pdb.org). PDB ID codes are the following: 5O4C the dark-conformation (a); 5NJ4 the  
277 dark conformation (b); 6ZHW the time-point  $\Delta t = 1$  ps; 6ZI4 the time-point  $\Delta t = 5$  ps (a);  
278 6ZID the time-point  $\Delta t = 5$  ps (b); 6ZI6 the time-point  $\Delta t = 20$  ps; 6ZI5 the time-point  $\Delta t =$   
279  $300$  ps (a); 6ZI9 the time-point  $\Delta t = 300$  ps (b); 6ZIA the time-point  $\Delta t = 8$   $\mu$ s. Difference  
280 Fourier electron density maps and stream files containing X-ray diffraction intensities are  
281 deposited at the CXI database (<http://www.cxidb.org/>) with identification number ID 161.

282

#### 283 **Competing Interests**

284 The authors declare no competing interests.

285

286

287

288

289

290

291 **REFERENCES**

- 292 1 Tenboer, J. *et al.* Time-resolved serial crystallography captures high-resolution  
293 intermediates of photoactive yellow protein. *Science* **346**, 1242-1246 (2014).
- 294 2 Emma, P. *et al.* First lasing and operation of an angstrom-wavelength free-electron  
295 laser. *Nat. Photon.* **4**, 641-647 (2010).
- 296 3 Marcus, R. A. & Sutin, N. Electron transfers in chemistry and biology. *Biochim.*  
297 *Biophys. Acta* **811**, 265-322 (1985).
- 298 4 Breton, J., Martin, J. L., Migus, A., Antonetti, A. & Orszag, A. Femtosecond  
299 spectroscopy of excitation energy transfer and initial charge separation in the reaction  
300 center of the photosynthetic bacterium *Rhodospseudomonas viridis*. *Proc. Natl. Acad.*  
301 *Sci. USA* **83**, 5121-5125 (1986).
- 302 5 Chan, C. K., DiMugno, T. J., Chen, L. X., Norris, J. R. & Fleming, G. R. Mechanism  
303 of the initial charge separation in bacterial photosynthetic reaction centers. *Proc. Natl.*  
304 *Acad. Sci. USA* **88**, 11202-11206 (1991).
- 305 6 Holten, D., Windsor, M. W., Parson, W. W. & Thornber, J. P. Primary photochemical  
306 processes in isolated reaction centers of *Rhodospseudomonas viridis*. *Biochim.*  
307 *Biophys. Acta* **501**, 112-126 (1978).
- 308 7 Vos, M. H., Rappaport, F., Lambry, J.-C., Breton, J. & Martin, J.-L. Visualization of  
309 coherent nuclear motion in a membrane protein by femtosecond spectroscopy. *Nature*  
310 **363**, 320-325 (1993).
- 311 8 Wang, H. *et al.* Protein dynamics control the kinetics of initial electron transfer in  
312 photosynthesis. *Science* **316**, 747-750 (2007).
- 313 9 Stowell, M. H. *et al.* Light-induced structural changes in photosynthetic reaction  
314 center: implications for mechanism of electron-proton transfer. *Science* **276**, 812-816  
315 (1997).

- 316 10 Wöhri, A. B. *et al.* Light-induced structural changes in a photosynthetic reaction  
317 center caught by Laue diffraction. *Science* **328**, 630-633 (2010).
- 318 11 Young, I. D. *et al.* Structure of photosystem II and substrate binding at room  
319 temperature. *Nature* **540**, 453-457 (2016).
- 320 12 Suga, M. *et al.* Light-induced structural changes and the site of O=O bond formation  
321 in PSII caught by XFEL. *Nature* **543**, 131-135 (2017).
- 322 13 Kern, J. *et al.* Structures of the intermediates of Kok's photosynthetic water oxidation  
323 clock. *Nature* **563**, 421-425 (2018).
- 324 14 Suga, M. *et al.* An oxyl/oxo mechanism for oxygen-oxygen coupling in PSII revealed  
325 by an x-ray free-electron laser. *Science* **366**, 334-338 (2019).
- 326 15 Nogly, P. *et al.* Retinal isomerization in bacteriorhodopsin captured by a femtosecond  
327 x-ray laser. *Science* **361**, eaat0094 (2018).
- 328 16 Pande, K. *et al.* Femtosecond structural dynamics drives the trans/cis isomerization in  
329 photoactive yellow protein. *Science* **352**, 725-729 (2016).
- 330 17 Coquelle, N. *et al.* Chromophore twisting in the excited state of a photoswitchable  
331 fluorescent protein captured by time-resolved serial femtosecond crystallography.  
332 *Nature Chem* **10**, 31-37 (2018).
- 333 18 Claesson, E. *et al.* The primary structural photoresponse of phytochrome proteins  
334 captured by a femtosecond X-ray laser. *Elife* **9**, e53514 (2020).
- 335 19 Hekstra, D. R. *et al.* Electric-field-stimulated protein mechanics. *Nature* **540**, 400-405  
336 (2016).
- 337 20 Wickstrand, C. *et al.* A tool for visualizing protein motions in time-resolved  
338 crystallography. *Struct Dyn* **7**, 024701 (2020).
- 339 21 Barends, T. R. *et al.* Direct observation of ultrafast collective motions in CO  
340 myoglobin upon ligand dissociation. *Science* **350**, 445-450 (2015).

- 341 22 Saito, K. *et al.* Deformation of chlorin rings in the Photosystem II crystal structure.  
342 *Biochemistry* **51**, 4290-4299 (2012).
- 343 23 Shelnut, J. A. *et al.* Nonplanar porphyrins and their significance in proteins. *Chem.*  
344 *Soc. Rev.* **27** 31-42 (1998).
- 345 24 Barkigia, K. M., Chantranupong, L., Smith, J. K. M. & Fajer, J. Structural and  
346 theoretical models of photosynthetic chromophores. Implications for redox, light-  
347 absorption properties and vectorial electron flow. *J. Am. Chem. Soc.* **110**, 7566-7567  
348 (1988).
- 349 25 Wraight, C. A. & Clayton, R. K. The absolute quantum efficiency of  
350 bacteriochlorophyll photooxidation in reaction centres of *Rhodospseudomonas*  
351 *spheroides*. *Biochim Biophys Acta* **333**, 246-260 (1974).
- 352 26 Dohse, B. *et al.* Electron transfer from the tetraheme cytochrome to the special pair in  
353 the *Rhodospseudomonas viridis* reaction center: effect of mutations of tyrosine L162.  
354 *Biochemistry* **34**, 11335-11343 (1995).
- 355 27 Steffen, M. A., Lao, K. & Boxer, S. G. Dielectric asymmetry in the photosynthetic  
356 reaction center. *Science* **264**, 810-816 (1994).
- 357 28 Najdanova, M., Grasing, D., Alia, A. & Matysik, J. Analysis of the Electronic  
358 Structure of the Special Pair of a Bacterial Photosynthetic Reaction Center by <sup>13</sup>C  
359 Photochemically Induced Dynamic Nuclear Polarization Magic-Angle Spinning NMR  
360 Using a Double-Quantum Axis. *Photochem Photobiol* **94**, 69-80 (2018).
- 361 29 Hasegawa, J.-Y. *et al.* Energetics of the Electron Transfer from Bacteriopheophytin to  
362 Ubiquinone in the Photosynthetic Reaction Center of *Rhodospseudomonas Viridis*:  
363 Theoretical Study. *J. Phys. Chem. B* **107**, 838-847 (2003).

364 30 LeBard, D. N., Martin, D. R., Lin, S., Woodbury, N. W. & Matyushov, D. V. Protein  
365 dynamics to optimize and control bacterial photosynthesis. *Chem. Sci.* **4**, 4127-4136  
366 (2013).

## 367 **FIGURE LEGENDS**

368

### 369 **Figure 1: Electron transfer steps of the photosynthetic reaction centre of *Bl. viridis*.**

370 Cartoon representation of the H, L, M and C subunits. Cofactors are shown in black including  
371 the special pair of bacteriochlorophylls (SP), two monomeric bacteriochlorophylls (BCh), two  
372 bacteriopheophytins (BPh), a tightly bound menaquinone ( $Q_A$ ), a mobile ubiquinone ( $Q_B$ ), a  
373 non-haem iron ( $Fe^{2+}$ ) and four haems. The approximate boundaries of the membrane are  
374 suggested in blue. The electron transfer pathway:  $SP \rightarrow BPh_L \rightarrow Q_A$  is referred to as the A-  
375 branch. Approximate timescales for the first two electron transfer events, from SP to  $BPh_L$   
376 and from  $BPh_L$  to  $Q_A$ , are depicted.

377

### 378 **Figure 2: Light-induced electron density changes in $RC_{vir}$ at the site of photo-oxidation.**

379 **a**, Experimental  $F_{obs}^{light} - F_{obs}^{dark}$  difference Fourier electron density map for  $\Delta t = 1$  ps. **b**,  
380 Difference Fourier electron density map for  $\Delta t = 5$  ps (data set a). **c**, Difference Fourier  
381 electron density map for  $\Delta t = 20$  ps. **d**, Difference Fourier electron density map for  $\Delta t = 300$   
382 ps (data set a). **e**, Principal component from SVD analysis of all seven experimental  
383 difference Fourier electron density maps. All maps are contoured at  $\pm 3.2 \sigma$  (blue, positive  
384 difference electron density; gold, negative difference electron density;  $\sigma$  is the root mean  
385 square electron density of the map). **f**, Relative amplitudes of difference electron density  
386 features integrated within a  $4.5 \text{ \AA}$  sphere<sup>20</sup> centred upon the  $RC_{vir}$  co-factors (Extended Data  
387 Fig. 3j). The colour bars represent: cyan,  $\Delta t = 1$  ps; blue,  $\Delta t = 5$  ps a and b (in that order);  
388 purple,  $\Delta t = 20$  ps; red,  $\Delta t = 300$  ps b and a (in that order); mustard,  $\Delta t = 8 \mu s$ .

389

390 **Figure 3: Light-induced electron density changes in RC<sub>vir</sub> within the menaquinone**

391 **binding pocket. a**, Experimental  $F_{\text{obs}}^{\text{light}} - F_{\text{obs}}^{\text{dark}}$  difference Fourier electron density map for

392  $\Delta t = 5$  ps (data set a). **b**, Difference Fourier electron density map for  $\Delta t = 300$  ps (data set a).

393 **c**, Principal component from SVD analysis of the first four experimental difference Fourier

394 electron density maps ( $\Delta t = 1$  ps, 5 ps (a), 5 ps (b), 20 ps). **d**, Principal component from SVD

395 analysis of the final three experimental difference Fourier electron density maps ( $\Delta t = 300$  ps

396 (a), 300 ps (b), 8  $\mu$ s). All maps are contoured at  $\pm 3.0 \sigma$  (blue, positive difference electron

397 density; gold, negative difference electron density). **e**, Difference Fourier electron density

398 map for  $\Delta t = 300$  ps (data set a) showing the protein immediately surrounding Q<sub>A</sub> and

399 contoured at  $\pm 3.5 \sigma$ . **f**, Superposition of the refined structures for the dark structure (yellow,

400 Q<sub>A</sub> in black) and  $\Delta t = 300$  ps (purple structure).

401

402 **Figure 4: Structural response of RC<sub>vir</sub> to electron transfer events. a**, Recurring

403 movements of C $\alpha$  atoms for  $\Delta t = 1$  ps quantified by full occupancy structural refinement

404 against 100 randomly resampled TR-SFX data sets. **b**, Recurring movements of C $\alpha$  atoms for

405  $\Delta t = 5$  ps (a) using the same representation. **c**, Recurring movements of C $\alpha$  atoms for  $\Delta t = 300$

406 ps (a) using the same representation. Recurring movements are represented as error weighted

407 mean ratios relative to 100 control structural refinements (Methods) coloured from grey (< 80

408 % of the maximum error weighted mean ratio) to red ( $\geq 95$  % of the maximum error weighted

409 mean ratio). An identical representation is given for all time points in Extended Data Fig. 7. **d**,

410 Movements of C $\alpha$  atoms estimated from QM/MM energy minimization calculations

411 associated with the SP photo-excited and all other cofactors in resting state: SP\*:BPh<sub>L</sub><sup>0</sup>:Q<sub>A</sub><sup>0</sup>

412 (Methods). **e**, Movements of C $\alpha$  atoms estimated from QM/MM energy minimization

413 calculations associated with the SP photo-oxidized and BPh<sub>L</sub> reduced: SP<sup>+1</sup>:BPh<sub>L</sub><sup>-1</sup>:Q<sub>A</sub><sup>0</sup>. **f**,

414 Movements of C $\alpha$  atoms estimated from QM/MM energy minimization calculations  
415 associated with SP photo-oxidized and Q<sub>A</sub> reduced: SP<sup>+1</sup>:BPh<sub>L</sub><sup>0</sup>:Q<sub>A</sub><sup>-1</sup>. Movements are  
416 coloured from grey (no movements) to red (maximum C $\alpha$  motions). Transmembrane helices  
417 are drawn as rods.

418 **METHODS**

419 *Protein production and purification*

420 The expression and purification of photosynthetic reaction centre from *Bl. viridis* cells was  
421 adapted from Wöhri et al.<sup>31</sup>. Cells were disrupted by three rounds of sonication followed by  
422 centrifugation in a JA20 rotor at 15000 rpm for 20 minutes to recover the membrane  
423 suspensions. Membranes were then purified by ultracentrifugation at 45000 rpm for 45 min in  
424 a Ti45 rotor. Membranes were homogenized in 20 mM Tris-HCl, pH 8.5 and diluted to  
425 OD<sub>1012</sub> = 10. Membranes were then solubilized in 4 % lauryldimehtylamine-N-oxide (LDAO)  
426 for 3 hours at room temperature. Unsolubilized membranes were removed by  
427 ultracentrifugation at 45000 rpm for 75 min in a Ti70 rotor. RC<sub>vir</sub> protein was purified by  
428 loading the supernatant onto a 250 ml POROS 50- $\mu$ m HQ ion-exchange medium equilibrated  
429 with wash buffer (20 mM Tris-HCl, pH 8.5, 1% LDAO). The column was washed with 2 l of  
430 wash buffer with 5 % elution buffer (20 mM Tris-HCL, pH 8.5, 1 M NaCl, 1 % LDAO) and  
431 eluted with an increasing concentration of elution buffer over 20 column volumes. Fractions  
432 with an A<sub>280</sub>/A<sub>830</sub> < 3.5 were pooled and concentrated in 100 kDa MW cut off concentration  
433 tubes (Vivaspin) to a volume of 10 ml. This was loaded in 5ml batches onto a HiPrep 26/60  
434 Sephacryl S-300 column (GE) equilibrated with SE buffer (20 mM Tris-HCl, pH 8.5, 100 mM  
435 NaCl, 0.1 % LDAO) and eluted into 1.8 ml fractions. Fractions with an A<sub>280</sub>/A<sub>830</sub> < 2.6 were  
436 pooled and concentrated, followed by a 20-fold dilution in final protein buffer (20mM  
437 NaH<sub>2</sub>PO<sub>4</sub>/Na<sub>2</sub>HPO<sub>4</sub>, pH 6.8, 0.1 % LDAO, 10  $\mu$ M EDTA) and then concentrated again to 20  
438 mg.ml<sup>-1</sup>. Samples were flash-frozen in liquid nitrogen and stored at -80 °C.

439

440 *Protein crystallization*

441 20  $\mu$ l sitting drops were set up with a 1:1 ratio of protein solution (10 mg.ml<sup>-1</sup>) and precipitant  
442 solution (3.6 M ammonium sulphate, 6 % heptane-1,2,3-triol, 20 mM NaH<sub>2</sub>PO<sub>4</sub>/Na<sub>2</sub>HPO<sub>4</sub>, pH

443 6.8) set up against a 1 ml reservoir of 2 M ammonium sulphate. Large crystals grew at 4 °C  
444 in 3 days. Crystals were harvested by pipette and crushed mechanically to create a seed stock  
445 by vortexing with seed beads for approximately 20 min with occasional cooling on ice<sup>32</sup>. For  
446 the XFEL experiment in April 2015 (run a) new 18.5 µl sitting drop vapour diffusion  
447 crystallization drops were set up in order to yield large numbers of micro-crystals. In these  
448 experiments the protein concentration was 8.5 mg.ml<sup>-1</sup> and a protein:precipitant concentration  
449 of 10:7.5 was used in the drops. 1 µl of undiluted crystal seed stock was spiked into the drops  
450 for a final v/v concentration of 5.4 %. Crystallization drops were then mixed by pipette and  
451 covered with a glass cover slide. Rod-like crystals grew over 5 days at 4 °C and were 10 – 20  
452 µm in the longest dimension. Microcrystals for the experiment in June 2016 (run b) were  
453 prepared as above, but with an additional round of microseeding using crushed microcrystals  
454 to seed an additional round of microcrystal growth<sup>32</sup>. Micro-crystals were harvested by pipette  
455 and concentrated up to three-fold by centrifugation at 1000 g for 1 min followed by removal  
456 of supernatant. These crystals were somewhat thicker and, while diffracting to higher-  
457 resolution, they highlighted the compromise inherent in TR-SFX since a lower excited-state  
458 occupancy was usually observed when working with crystals of higher optical density.

459

#### 460 *Sample injection and data collection*

461 Microcrystals were transferred from Eppendorf tubes to a sample reservoir using a syringe  
462 and passing the microcrystal slurries through a stainless steel 20 µm filter (VICI AG  
463 International) or a 20µm nylon filter (Sysmex). The reservoir was loaded into a temperature  
464 controlled rocking chamber and injected into the XFEL through a GDVN<sup>33</sup> using an internal  
465 diameter of 75 µm. The microjet used a microcrystal suspension flow rate of 20 µl.min<sup>-1</sup> and  
466 was focused to a 10 µm diameter using helium gas. The X-ray beam was aligned to interact

467 with the liquid jet as close to the tip of the GDVN as practical and before Rayleigh breakup of  
468 the microjet.

469

470 Diffraction data were collected at 293 K at the CXI beam line<sup>34</sup> of the LCLS XFEL during  
471 beamtime awarded in April 2015 (run a) and June 2016 (run b). Diffraction data were  
472 recorded on a Cornell-SLAC Pixel Array detector<sup>35</sup>. The X-ray wavelengths and equivalent  
473 pulse energies were 1.89 Å (6.56 keV) in 2015 and 1.31 Å (9.49 keV) in 2016. An X-ray  
474 pulse duration of 36 fs was used in 2015 and 45 fs in 2016. The XFEL beam was focused to a  
475  $3 \mu\text{m}^2$  spot for both experiments. The detector was located 89 mm from the microjet in 2015  
476 and 145 mm from the microjet in 2016. Diffraction data were collected at a repetition rate of  
477 120 Hz from microcrystals that were not exposed to any optical laser pump (dark-state) and  
478 for five time points corresponding to  $\Delta t = 1 \text{ ps}$ , 5 ps, 20 ps, 300 ps and 8  $\mu\text{s}$  after photo-  
479 excitation. The time points  $\Delta t = 5 \text{ ps}$  and 300 ps were repeated in both 2015 and 2016 and are  
480 referred to as data sets a and b respectively.

481

#### 482 *Laser photoexcitation*

483 An optical Ti:Sa pump laser 150 fs in duration was focused into a spot size of 190  $\mu\text{m}$  FWHM  
484 ( $323 \mu\text{m}^2$ ) and aligned to overlap with the LCLS X-ray pulse. The LCLS timing-tool<sup>36</sup>  
485 provided a timing accuracy of  $\pm 200 \text{ fs}$  for the time point,  $\Delta t$ , between the arrival of the  
486 optical pump laser and the X-ray probe. A pump-laser wavelength of 960 nm was used to  
487 photo-excite  $\text{RC}_{\text{vir}}$  microcrystals, and this wavelength is at the absorption maximum of the  
488 special pair ( $\epsilon_{960} \approx 100\,000 \text{ M}^{-1} \cdot \text{cm}^{-1}$ ). The pump laser energy per pulse was 11.8  $\mu\text{J}$  in April  
489 2015 and 11.0  $\mu\text{J}$  in June 2016. For an idealized Gaussian beam, 86.5 % of this light will pass  
490 through a spot with diameter  $1/e^2$  and 50 % of this light will pass through a spot with diameter  
491 FWHM. Thus the average fluence within the FWHM spot can be estimated as 25  $\text{mJ}/\text{cm}^2$  and

492 23 mJ/cm<sup>2</sup> which equates to a pump-laser power-density of 138 GW/cm<sup>2</sup> for the 2015  
493 experiment and 129 GW/cm<sup>2</sup> for the 2016 experiment. This calculation defines the units used  
494 throughout to specify the laser power-density. Both values are above 30 GW/cm<sup>2</sup> to 100  
495 GW/cm<sup>2</sup> that has been recommended as an upper threshold to avoid nonlinear effects in  
496 bacteriorhodopsin.<sup>37,38</sup>

497

498 Extreme non-linear absorption was observed as ultrafast sample heating in time-resolved X-  
499 ray scattering studies of RC<sub>vir</sub> when pumped with 800 nm light.<sup>39</sup> When using 800 nm to  
500 photo-excite RC<sub>vir</sub> it is the BCh cofactors (rather than the SP) which absorb light ( $\epsilon_{800} \approx$   
501 180 000 M<sup>-1</sup>.cm<sup>-1</sup>). The pump-laser fluence used in that study<sup>39</sup> was 1560 GW/cm<sup>2</sup>. Ultrafast  
502 sample heating within a GDVN liquid microjet has also been measured as a function of the  
503 800 nm pump-laser fluence using time-resolved X-ray scattering (Fig. 28 of reference<sup>40</sup>).  
504 These measurements show that the energy deposited into RC<sub>vir</sub> samples is proportional to the  
505 pump-laser fluence (a linear response) up to 270 GW/cm<sup>2</sup> and that the measured heating then  
506 varies quadratically (a non-linear response) above a pump-laser fluence of 355 GW/cm<sup>2</sup>. Thus  
507 either an idealized assumptions of a perfectly aligned Gaussian beam may not be realistic,  
508 and/or large losses occur as the incoming laser pulse is reflected from the surface of a GDVN  
509 liquid microjet, and/or a thresholds<sup>37,38</sup> of 30 GW/cm<sup>2</sup> to 100 GW/cm<sup>2</sup> do not apply RC<sub>vir</sub>  
510 when photo-excited at 800 nm. When 960 nm light is used to photo-excite the SP of RC<sub>vir</sub> it is  
511 likely more difficult to induce non-linear effects because the photo-excited state SP\* has an  
512 absorption maximum red-shifted 70 nm relative to the ground state<sup>41</sup> and hole-burning<sup>42</sup> has  
513 been observed in RC<sub>vir</sub> such that SP\* is effectively transparent to the incoming light.  
514 Moreover, the absorbance of RC<sub>vir</sub> at 960 nm is only 56 % of its absorbance at 800 nm and  
515 therefore non-linear effects are likely to arise at higher power densities when using 960 nm  
516 rather than 800 nm to photo-excite RC<sub>vir</sub>. Non-linear ultrafast heating<sup>40</sup> is observed in RC<sub>vir</sub>

517 delivered using a GDVN liquid microjet and photo-excited at 800 nm only above a power-  
518 density of 355 GW/cm<sup>2</sup>. Therefore the 960 nm pump-laser power-densities of 138 GW/cm<sup>2</sup>  
519 and 129 GW/cm<sup>2</sup> used in this work are below where non-linear effects may reasonably be  
520 anticipated. These conclusions are supported by time-resolved IR spectroscopy measurements  
521 (Extended Data Fig. 1).

522

### 523 *Time-resolved infrared spectroscopy*

524 Time-resolved vibrational spectroscopy measurements were performed with a near infrared  
525 (NIR) pump and mid-infrared (IR) probe setup using a regenerative amplifier (Spitfire Ace,  
526 Spectra Physics) to deliver pulses centred at 800 nm (1.2 mJ, 5 kHz). The amplifier output is  
527 used to pump a TOPAS-TWINS (Light Conversion) capable of generating tuneable  
528 femtosecond pulses at two different wavelengths. One path was used to generate mid-infrared  
529 probe light centred at 6000 nm via difference frequency generation whereas the other path  
530 generated 960 nm pump pulses via second harmonic generation of the idler beam. The 960  
531 nm beam was chopped to 2.5 kHz and delayed in time relative to the probe pulses using an  
532 optical delay line. Two weak replicas derived from the midIR beam were used as probe and  
533 corresponding reference. Both probe and reference were dispersed in a Horiba spectrograph  
534 (grating with 75 gr/mm) and detected and integrated on a double-row MCT array with 64  
535 pixels each on a shot-to-shot basis using a commercial detection system (Infrared Systems).  
536 Samples of RC<sub>vir</sub> were prepared in a customized cell by enclosing ca. 15 uL of solution (RC<sub>vir</sub>  
537 at ca. 0.4 mM in D<sub>2</sub>O buffer) between two 2 mm thick CaF<sub>2</sub> windows separated by a 25 μm  
538 spacer. Probe and reference beams were focused at the sample position and collimated using  
539 90° off-axis parabolic mirrors. The pump beam was focused using a 30-cm lens and  
540 overlapped with the probe beam at its focus. The sample cell was placed where pump and  
541 probe beams meet and translated continuously perpendicular to the beam direction during data

542 acquisition. The focal spot size of the pump beam was determined using knife-edge scans and  
543 yielded perpendicular  $1/e^2$  radii of 57  $\mu\text{m}$  and 56  $\mu\text{m}$ . Different pump fluences were adjusted  
544 using reflective neutral density filters (Edmund Optics). For each fluence, twelve repeats over  
545 five time points (1000 pump shots per time point and repeat, at delays of -50, 1, 2, 5 and 300  
546 ps) were recorded and less than 5% of shots were rejected during data treatment. Signals were  
547 calculated by subtracting consecutive pump-on from pump-off shots followed by application  
548 of the noise reduction algorithm.<sup>43,44</sup> The spectral resolution is  $< 5 \text{ cm}^{-1}$ . The results of these  
549 measurements are presented in Extended Data Fig. 1.

550

#### 551 *Data processing*

552 Images containing more than 20 diffraction spots were identified as diffraction hits by  
553 Cheetah.<sup>45</sup> Cheetah converted the raw detector data into the HDF5 format and data were then  
554 processed using the software suite CrystFEL version 0.6.2.<sup>46,47</sup> Crystals were indexed using a  
555 tetragonal unit cell ( $a = b = 226.4 \text{ \AA}$ ,  $c = 113.7 \text{ \AA}$ ,  $\alpha = \beta = \gamma = 90^\circ$ ). Scaling and merging were  
556 performed using Monte Carlo methods using the same software. Data from the dark state and  
557 photo-excited states were scaled together using the custom dataset splitting option in the  
558 CrystFEL partialator module. Structure factors were calculated from merged intensities by the  
559 CCP4 module TRUNCATE<sup>48</sup> and molecular replacement was performed using the CCP4  
560 module Phaser<sup>49</sup> using the ground-state  $\text{RC}_{\text{vir}}$  structures solved with XFEL radiation (PDB  
561 codes 5O4C and 5NJ4) as a search models. Statistics for data collection and refinement are  
562 detailed in Extended Data Table 1.

563

#### 564 *Electron density difference maps*

565 Isomorphous  $|F_{\text{obs}}|^{\text{light}} - |F_{\text{obs}}|^{\text{dark}}$  difference Fourier electron density maps were calculated using  
566 the refined dark state structures for phases with the time-points  $\Delta t = 5 \text{ ps}$  (data set a) and 300

567 ps (data set a) calculated against data and coordinates using the pdb entry 5O4C whereas the  
568 time point with the time-points  $\Delta t = 1$  ps, 5 ps (data set b), 20 ps, 300 ps (data set b) and 8  $\mu$ s  
569 were calculated against data and coordinates using the pdb entry 5NJ4. Thus all difference  
570 electron density map calculations used only data collected during the same experiment.  
571 Difference Fourier electron density maps represent measured changes in X-ray diffraction  
572 intensities as changes in electron density without bias towards the photo-activated state's  
573 structural model. The technique is extremely sensitive to small changes in electron density<sup>50</sup>  
574 and reveals more subtle features than are apparent from  $2mF_{\text{obs}}-DF_{\text{calc}}$  electron density maps  
575 alone ( $m$  is the figure of merit and  $D$  is estimated from coordinate errors). A Bayesian  
576 weighting calculation script<sup>51</sup> using CNS software<sup>52</sup> was also used to analyse the difference  
577 Fourier electron density maps. In this procedure structure factor amplitude differences were  
578 weighted by the product of the figure of merit of the ground state structure reflections and of a  
579 weighting term,  $w$  (Equation 14 of reference<sup>53</sup>), which was calculated  
580 using Bayesian statistics developed to improve signal to noise.<sup>53</sup> For six of seven data-sets the  
581 recurring difference electron density features were slightly strengthened by this step. The  
582 exception was the time-point  $\Delta t = 8$   $\mu$ s which has difference electron density feature that are  
583 weaker than for the other maps (Fig. 2f) and appears due to a lower occupancy of the charge  
584 separated state in these microcrystals. It is possible that a fraction of the photo-oxidized SP<sup>-</sup>  
585 population is reduced from the C-subunit by  $\Delta t = 8$   $\mu$ s, which is longer than the time-scale of  
586 this electron transfer step.<sup>26</sup> However, no efforts were made to reduce the C-subunit when  
587 preparing microcrystals and a similar occupancy ( $30\% \pm 5\%$ ) is observed to persist in time-  
588 resolved spectroscopy measurements on crystals for up to millisecond delays.<sup>10</sup>

589

590 *Singular value decomposition*

591 SVD analysis of difference Fourier electron density maps was performed using an in-house  
592 code written in python that is based upon an approach previously described.<sup>54</sup> As has been  
593 discussed,<sup>55</sup> SVD may serve as a noise-filter to enhance the signal across a sequence of  
594 difference Fourier electron density maps. This step contains the assumption that the overall  
595 mechanism is linear and that changes in electron density are similar over the selected time-  
596 windows. When applying SVD we evaluate the expression  $[U, \Sigma, V] = \text{SVD}(A)$ , where A is a  
597 matrix of n difference Fourier electron density maps containing m elements; U is an  $n \times n$   
598 unitary matrix;  $\Sigma$  is an  $n \times m$  rectangular matrix containing n diagonal elements (the singular  
599 values) arranged in decreasing order and all other matrix elements are zero; and the first right  
600 singular vector (the first row of the matrix V) is referred to as the principal component.  
601 Results from SVD analysis of all seven electron density maps are presented in Fig. 2e and  
602 Extended Data Fig. 3l,m. Results from SVD analysis deriving from the first four time-points  
603 ( $\Delta t = 1$  ps, 5 ps a and b, 20 ps) and the last three time-points ( $\Delta t = 300$  ps a and b, 8  $\mu$ s) are  
604 shown in Fig. 3c,d; Extended Data Fig. 3h,i; Extended Data Fig. 5h,i; Supplementary Videos  
605 1 and 2. This separation of the maps is motivated by the fact that photo-activated RC<sub>vir</sub>  
606 molecules have menaquinone oxidized for the first sub-set of time-points yet most  
607 menaquinone molecules of photo-activated RC<sub>vir</sub> are reduced for the second sub-set of time-  
608 points.

609

#### 610 *Structural refinement of photo-excited states*

611 Isomorphous  $|F_{\text{obs}}|^{\text{light}} - |F_{\text{obs}}|^{\text{dark}}$  difference Fourier electron density maps were inspected in  
612 COOT. Structural refinement was performed using Phenix.<sup>56</sup> A model was first placed within  
613 the unit cell using rigid body refinement followed by multiple rounds of partial-occupancy  
614 refinement where the SP, BCh<sub>L</sub>, BPh<sub>L</sub>, Q<sub>A</sub>, portions of TM helices E<sub>L</sub>, D<sub>L</sub>, E<sub>M</sub> and D<sub>M</sub>, as well  
615 as connecting loops, and additional residues near cofactors (L153-178, L190, L230, L236-

616 248, M193-221, M232, M243-253, M257-266) were allowed to adopt a second conformation  
617 with 30 % occupancy and the dark-state structure (pdb entry 5O4C) was held fixed. The  
618 occupancy of 30 % was chosen by assessing the results from partial occupancy refinement  
619 when the occupancy was allowed to vary and was imposed for all structural refinements for  
620 consistency. Results from structural refinement were compared against the difference electron  
621 densities and some manual adjustments were made using COOT.<sup>57</sup> Refinement statistics are  
622 displayed in Extended Data Table 1. Validation of structure geometry was performed using  
623 MOLPROBITY<sup>58</sup> and PROCHECK.<sup>59</sup> Structural changes were also validated by calculating  
624 simulated difference Fourier electron density maps from the refined structures<sup>10,20</sup> (Extended  
625 Data Figs. 2i and 4j).

626

#### 627 *Structural analysis of large-scale protein motions*

628 The high multiplicity of SFX data was exploited for structural analysis by randomly selecting  
629 a sub-set of experimental observations from within each SFX data-set to create 100 separate  
630 (but not independent) serial crystallography data-sets for the two resting state data-sets and  
631 the seven photo-activated data-sets, amounting to 900 resampled data-sets in total. For each of  
632 these resampled data-sets the mean and uncertainty estimates ( $\sigma$ ) for every unique Bragg  
633 reflection were determined. Structural refinement over a cycle of 100 rigid body and 100  
634 isotropic restrained refinements with all atoms allowed to move and with every atom having  
635 100 % occupancy were then performed against each of these 900 resampled data-sets using  
636 pdb entry 5NJ4 as a starting model.  $R_{\text{free}}$  values ranging from 22.1 % to 23.1% were  
637 recovered. Coordinate errors associated with each individual structural refinement are  
638 estimated<sup>60</sup> to be  $\leq 0.2$  Å.

639

640 The distances between the Ca atoms of the photo-activated and resting RC<sub>vir</sub> structures were  
 641 compared pairwise using the miller package of CCTBX.<sup>61</sup> A 100×100 Euclidian distance  
 642 matrix was then calculated for every Ca atom and every time point according to:  $\Delta r_{ij}^{\Delta t, \text{dark}} =$   
 643  $|\mathbf{r}_i^{\Delta t} - \mathbf{r}_j^{\text{dark}}|$ , where  $i$  and  $j$  vary from 1 to 100 and denote resampled dataset numbers,  $\Delta r_{i,j}$   
 644 depicts the distance separating the Ca coordinates of datasets  $i$  and  $j$ , and  $\mathbf{r}_i^{\Delta t}$  and  $\mathbf{r}_j^{\text{dark}}$  are the  
 645 refined coordinates obtained from the photo-activated or dark structures, respectively. A  
 646 second order Taylor series expansion was then used to estimate the mean and error associated  
 647 with the ratio  $\Delta r_{ij}^{\Delta t, \text{dark}} / \Delta r_{ij}^{\text{dark, dark}}$  arising from coordinate variations within each set of 100  
 648 structural refinements. This expansion leads to the expression:

$$649 \quad \text{Error weighted mean ratio} = \langle \Delta r_{ij}^{\text{state, dark}} \rangle / \langle \Delta r_{ij}^{\text{dark, dark}} \rangle$$

$$650 \quad - \text{var}(\Delta r_{ij}^{\text{dark, dark}}) \times \langle \Delta r_{ij}^{\text{state, dark}} \rangle / \langle \Delta r_{ij}^{\text{dark, dark}} \rangle^3 + \text{cov}(\Delta r_{ij}^{\text{state, dark}}, \Delta r_{ij}^{\text{dark, dark}}) / \langle \Delta r_{ij}^{\text{dark, dark}} \rangle^2$$

651 where  $\langle X \rangle$  is the mean of the set X,  $\text{var}(X)$  is the variance of the set X, and  $\text{cov}(X, Y)$  is the  
 652 covariance of two sets X and Y. The resulting error weighted mean ratios are represented in  
 653 Fig. 4A to 4C and Extended Data Fig. 7 in which movements are coloured from grey  
 654 (movements  $\leq 80\%$  of the maximum ratio) to red (movements  $\geq 95\%$  of the maximum ratio).  
 655 Full occupancy structural refinement avoided systematic bias in this analysis arising from  
 656 partial occupancy structural refinement with a single dark-conformation held fixed, but at the  
 657 cost of underestimating the magnitude of light-induced conformational changes. Despite this  
 658 limitation, this analysis extracted recurring structural motions that evolve with time (Fig. 4a-c  
 659 and Extended Data Fig. 7, Supplementary Video 3) and in a manner that is both consistent  
 660 with the known time-scales of the electron transfer reactions (Fig. 1) and theoretical  
 661 predictions (Fig. 4d-f, Supplementary Video 4).

662

663 *Tests of the statistical significance of recurring difference electron density features*

664 For each of the seven experimental difference Fourier electron density maps ( $\Delta t = 1$  ps, 5 ps  
 665 (data set a), 5 ps (data set b), 20 ps, 300 ps (data set b), 300 ps (data set a), 8  $\mu$ s) a lower-  
 666 pedestal of  $3.0 \sigma$  was applied such that all electron density with an amplitude  $< 3.0 \sigma$  was set  
 667 to zero. Both positive and negative difference electron densities were then integrated within a  
 668  $4.5 \text{ \AA}$  radius sphere about a chosen coordinate (Extended Data Fig. 3j) as described for the  
 669 analysis of TR-SFX data recorded from bacteriorhodopsin.<sup>20</sup> These positive (A+) and  
 670 negative (A-) integrated difference electron density amplitudes were merged to yield a single  
 671 amplitude according to:  $A(\mathbf{r}) = ((A^+)^2 + (A^-)^2)^{1/2}$  about the centre of integration  $\mathbf{r}$ . The results of  
 672 this analysis are presented in Fig. 2f where six centres of integration,  $\mathbf{r}$ , are chosen as: the  
 673 centre of the BPh<sub>M</sub> ring; the magnesium atom of BCh<sub>M</sub>; the mid-point between the two  
 674 magnesium atoms of the two SP bacteriochlorophylls; the magnesium atom of BCh<sub>L</sub>; the  
 675 centre of the BPh<sub>L</sub> ring; and the centre of the ketone containing six-carbon ring of  
 676 menaquinone Q<sub>A</sub>.

677

678 For tests of statistical significance (Extended Data Table 3), this set was complemented by the  
 679 addition of amplitudes extracted by integration about the iron atoms of haem<sub>1</sub>, haem<sub>2</sub>, haem<sub>3</sub>  
 680 and haem<sub>4</sub> to create a set of ten amplitudes for each of the seven time points:

681  $[A(\text{BPh}_M), A(\text{BCh}_M), A(\text{SP}), A(\text{BCh}_L), A(\text{BPh}_L), A(\text{Q}_A), A(\text{H}_1), A(\text{H}_2), A(\text{H}_3), A(\text{H}_4)]_{\Delta t}$

682 arranged as a  $10 \times 7$  element matrix. Control “noise only”  $|F_{\text{obs}}|^{\text{dark}} - |F_{\text{obs}}|^{\text{dark}}$  isomorphous  
 683 difference Fourier electron density maps were calculated by first selecting sixteen resampled  
 684 data-sets from the set of 100 generated from the 2015 RC<sub>vir</sub> dark data, and sixteen resampled  
 685 data-sets from the set of 100 generated from the 2016 RC<sub>vir</sub> dark data. Eight  $|F_{\text{obs}}|^{\text{dark}} - |F_{\text{obs}}|^{\text{dark}}$   
 686 isomorphous difference Fourier electron density maps were then calculated by pair-wise  
 687 comparisons between the sixteen resampled data-sets of the 2015 data, and another eight  
 688 difference Fourier electron density maps were calculated by pairwise-comparisons of the

689 sixteen resampled data-sets of the 2016 data. Seven control difference Fourier electron density  
690 maps were then randomly selected from the set of sixteen “noise-only” maps, difference  
691 electron density values with an amplitude lower than  $3\sigma$  were set to zero, and a set of  
692  $[A(\mathbf{r}, \text{dark-dark})]$  were created by integrating the remaining difference electron density within  
693 a 4.5 Å radius sphere centred upon the  $\text{RC}_{\text{vir}}$  cofactors as described above. A two-sample  $t$ -  
694 test was then performed in MATLAB to determine if the set of seven time-dependent  
695 amplitudes  $[A(\mathbf{r}, \Delta t)]$  and the set of seven “noise-only” amplitudes  $[A(\mathbf{r}, \text{dark-dark})]$  were  
696 indistinguishable from one another (the null hypothesis). The  $t$ -tests were then repeated 1000  
697 times by randomly selecting a different combination of seven control amplitudes  $[A(\mathbf{r}, \text{dark-}$   
698  $\text{dark})]$  from the sixteen “noise-only” difference Fourier electron density maps calculated  
699 above (of  $16!/(9! \times 7!) = 11440$  possible different combinations of the 16 control maps). The  
700 results of this analysis are summarized in Extended Data Table 3 and show that, when a  
701 threshold of  $p \leq 0.001$  is applied, the difference electron density amplitudes associated with  
702 the SP cannot be ascribed to noise. When a threshold of  $p \leq 0.0125$  is applied and the last  
703 three time-points ( $\Delta t = 300$  ps (a), 300 ps (b), 8  $\mu\text{s}$ ) are examined as a set, the difference  
704 electron density amplitudes associated with the SP, BCh<sub>L</sub> and Q<sub>A</sub> cannot be ascribed to noise.  
705 Conversely, the set of difference electron density amplitudes associated with most other co-  
706 factors, as well as all sets of difference electron density amplitudes generated from noise-only  
707 maps, are indistinguishable from noise according to the results of this two sample  $t$ -test  
708 (Extended Data Table 3).

709

#### 710 *QM/MM Geometry optimizations*

711 Initial coordinates were taken from PDB databank entry 5O4C and missing residues and co-  
712 factor segments were retrieved from PDB entry 1PRC.<sup>62</sup> Protonation states of residues were  
713 chosen based on their reference  $\text{pK}_a$  values and structural criteria such as hydrogen bond

714 interactions. After the addition of protons to the structure, a 200 step steepest descent  
715 geometry optimization was performed with Gromacs 4.5<sup>63</sup> to relax these coordinates. During  
716 this optimization the positions of the heavy atoms were constrained to their positions in the x-  
717 ray structure. As in previous work, the interactions were modelled with the Amber03 force-  
718 field.<sup>64,65</sup> Non-bonded Coulomb and Lennard-Jones interactions were evaluated without  
719 periodic boundary conditions (PBC) and using infinite cut-offs.

720

721 After relaxing hydrogens with molecular mechanics (MM) optimization, we performed  
722 several Quantum Mechanics (QM)/MM geometry optimizations of all atoms in the reaction  
723 centre, using the interface between the TeraChem quantum chemistry package<sup>66,67</sup> and  
724 Gromacs 4.5.<sup>63</sup> These optimizations were also performed without PBC and with infinite cut-  
725 offs for the Coulomb and Lennard-Jones interactions. The QM subsystems (Extended Data  
726 Fig. 6a-c) were modelled with unrestricted DFT. In these DFT calculation we used the PBE0  
727 functional<sup>68</sup> in combination with the LANL2DZ basis set.<sup>69</sup> Empirical corrections to  
728 dispersion energies and interactions were introduced with Grimme's DFT-D3 model.<sup>70</sup> The  
729 remainder of the protein, including crystal water molecules, was modelled with the Amber03  
730 force-field,<sup>64,65</sup> in combination with the TIP3P water model.<sup>71</sup> We searched for minimum-  
731 energy geometries in all relevant oxidation states of the system using the limited-memory  
732 Broyden-Fletcher-Goldfarb-Shannon quasi-Newton optimization algorithm.

733

734 The goal of these optimization steps was to characterize the structural relaxation of the protein  
735 in response to changes in the electronic states of the cofactors along the A-branch of the  
736 photo-induced electron transfer process. We therefore examined the following electronic  
737 configurations:

738 i. All cofactors in their resting states:  $SP^0$ ,  $BPh_L^0$ ,  $Q_A^0$

739 ii. Special pair photo-excited, other cofactors in resting state:  $SP^*$ ,  $BPh_L^0$ ,  $Q_A^0$

740 iii. Special pair photo-oxidized,  $BPh_L$  reduced:  $SP^{+1}$ ,  $BPh_L^{-1}$ ,  $Q_A^0$

741 iv. Special pair photo-oxidized,  $Q_A$  reduced:  $SP^{+1}$ ,  $BPh_L^0$ ,  $Q_A^{-1}$

742 Since including all co-factors into one large QM-region is computationally too demanding, we  
743 performed the optimizations with a different QM subsystem for each co-factor, including  
744 nearest residues, in all relevant electronic states. The structural response to the change in  
745 electronic state (Fig. 4d-f) was obtained by comparing the optimized geometries and potential  
746 energies in the various oxidation states.

747

748 To quantify the effect of photo-absorption by the special pair (SP, i to ii) we first optimized  
749 the resting state with the SP plus nearby residues in the QM region (Extended Data Fig. 6a),  
750 described at the PBE0/LANL2DZ level of theory plus D3 dispersion corrections. This  
751 structure was used as a reference for the optimized structures in the excited state ( $SP^*$ , ii) and  
752 after photo-oxidation ( $SP^{+1}$ , iii). Using the same QM/MM subdivision, we optimized the  
753 system in the first singlet excited state ( $S_1$ ) by switching the QM description to the Time-  
754 dependent DFT within the Tamm-Dancoff approximation,<sup>72</sup> and in the photo-oxidized state  
755 by switching the spin state of the electronic wave function to the lowest energy doublet state  
756 ( $D_0$ ). In the QM/MM optimization of the  $D_0$  state of the SP, we modelled the  $BPh_L$  with point  
757 charges representing the reduced state of that co-factor. Only very modest protein structural  
758 changes were associated with the optimized geometries with the SP in the  $S_1$  and  $D_0$  relative  
759 to the reference structure in the resting state ( $S_0$ ). Likewise, we also optimized the geometry  
760 of the protein with the  $BPh_L$  and nearby residues in the QM region (Extended Data Fig. 6d) in  
761 both the lowest energy singlet ( $S_0$ , i) and doublet ( $D_0$ , reduced, iii) states. In the optimization  
762 of the  $D_0$  state of  $BPh_L$ , the partial charges on the SP were changed to reflect its photo-

763 oxidized ( $D_0$ ,  $SP^{+1}$ ) state. Again the structural response is rather minor, as the geometries are  
764 very similar (Extended Data Fig. 6e).

765

766 In the next step of the electron transfer process, the electron transfers from  $BPh_L$  to  $Q_A$  (iv).  
767 We optimized the protein with  $Q_A$  plus its immediate environment, including the non-heme  
768  $Fe^{2+}$  site, in the QM region. The optimized structures in the resting and reduced states are  
769 compared in Extended Data Fig. 6f. Reduction of  $Q_A$  from menaquinone to (deprotonated)  
770 semiquinone induces significant structural changes in the  $Q_A$  binding pocket. In line with the  
771 difference densities observed at 300 ps after photo-excitation, the hydrogen bond between the  
772  $Q_A$  carbonyl and His217<sub>M</sub> reduces by 0.17 Å. We suggest that the reduction of this hydrogen  
773 bond helps stabilizing the negative charge on the  $Q_A$ .

774

775 To quantify the overall structural response to the electron transfers, we computed the  
776 displacements of the atoms in the various states (ii-iv) with respect to the structure of resting  
777 state (i) and recorded these displacements as B-factors to the pdb coordinate file of the resting  
778 state. Because only one co-factor was included in the QM region of our QM/MM  
779 optimizations, we summed up the displacements of both QM/MM optimizations of each redox  
780 state. Fig. 4d-f represents these displacements as colours.

781

### 782 *Stabilization energies*

783 To estimate the energetic effects of the protein structural changes on the electron transfer  
784 process, we computed the adiabatic and vertical electron affinities for  $Q_A$  in isolation and in  
785 the optimized QM/MM protein models. These energies are shown schematically in Extended  
786 Data Fig. 6g,h. For the neutral  $Q_A$  in vacuum, the electron affinity *without* structural  
787 relaxation is 164.5 kJ.mol<sup>-1</sup> (vertical electron affinity, VEA). Structural relaxation in response

788 to adding the electron increases the affinity further by  $24 \text{ kJ.mol}^{-1}$ , so that the energy  
789 difference between the neutral reactant minimum on the one hand and the reduced product  
790 minimum is  $188.5 \text{ kJ.mol}^{-1}$  (adiabatic electron affinity, AEA) on the other hand. The  
791 calculated AEA is in good agreement with results from previous computations,<sup>29</sup> but is an  
792 overestimation with respect to the experimental value for the related 1,4-naphthoquinone ( $175$   
793  $\text{kJ.mol}^{-1}$ ).<sup>73</sup> Inside the protein environment, the VEA is much higher ( $258 \text{ kJ.mol}^{-1}$ ), part of  
794 which we attribute to the electrostatic interaction between the reduced  $Q_A$  co-factor with the  
795 positively charged  $\text{Fe}^{2+}$  ligand site. Structural relaxation of both the  $Q_A$  cofactor and the  
796 protein environment increases the electron affinity by  $60 \text{ kJ.mol}^{-1}$  to yield an AEA of  $318$   
797  $\text{kJ.mol}^{-1}$ . Thus, the results of the computations suggest that the structural response of the  
798 protein adds another  $36 \text{ kJ.mol}^{-1}$  to the intrinsic relaxation energy of  $Q_A$  ( $24 \text{ kJ.mol}^{-1}$  in  
799 vacuum) as concluded in earlier computations.<sup>29</sup> We note that in this analysis we focussed  
800 only on the effect of the structural response on the affinity of  $Q_A$ . To estimate the *total*  
801 reaction energy associated with the photo-induced electron transfer process from the SP to  
802  $Q_A$ , we also need the absolute energies of the neutral, photo-excited and oxidized states of the  
803 SP as well as the neutral and reduced states of  $\text{BPh}_L$ . However, since these energies were not  
804 computed with identical QM/MM setups, we do not provide an accurate estimate here.

805

806

807

808

809 **METHODS REFERENCES**

810

- 811 31 Wöhri, A. B. *et al.* Lipidic sponge phase crystal structure of a photosynthetic reaction  
812 center reveals lipids on the protein surface. *Biochemistry* **48**, 9831-9838 (2009).
- 813 32 Dods, R. *et al.* From Macrocrystals to Microcrystals: A Strategy for Membrane  
814 Protein Serial Crystallography. *Structure* **25**, 1461-1468 (2017).
- 815 33 DePonte, D. P. *et al.* Gas dynamic virtual nozzle for generation of microscopic droplet  
816 streams. *J. Phys. D: Appl. Phys.* **41**, 195505 (2008).
- 817 34 Liang, M. *et al.* The Coherent X-ray Imaging instrument at the Linac Coherent Light  
818 Source. *J Synchrotron Radiat* **22**, 514-519 (2015).
- 819 35 Hart, P. *et al.* The CSPAD megapixel x-ray camera at LCLS. *Proc. SPIE* **8504C**,  
820 85040C-85011 (2012).
- 821 36 Harmand, M. *et al.* Achieving few-femtosecond time-sorting at hard X-ray free-  
822 electron lasers. *Nature Phot.* **7**, 215-218 (2013).
- 823 37 Nass Kovacs, G. *et al.* Three-dimensional view of ultrafast dynamics in photoexcited  
824 bacteriorhodopsin. *Nat Commun* **10**, 3177 (2019).
- 825 38 Miller, R. J. D., Pare-Labrosse, O., Sarracini, A. & Besaw, J. E. Three-dimensional  
826 view of ultrafast dynamics in photoexcited bacteriorhodopsin in the multiphoton  
827 regime and biological relevance. *Nat Commun* **11**, 1240 (2020).
- 828 39 Arnlund, D. *et al.* Visualizing a protein quake with time-resolved X-ray scattering at a  
829 free-electron laser. *Nat Methods* **11**, 923-926 (2014).
- 830 40 Arnlund, D. *X-ray free-electron laser based methods for structural and ultrafast*  
831 *dynamics studies of a photosynthetic reaction centre* PhD thesis, University of  
832 Gothenburg, (2014).

- 833 41 Fleming, G. R., Martin, J. L. & Breton, J. Rates of primary electron transfer in  
834 photosynthetic reaction centres and their mechanistic implications. *Nature* **333**, 190-  
835 192 (1988).
- 836 42 Meech, S. R., Hoff, A. J. & Wiersma, D. A. Role of charge-transfer states in bacterial  
837 photosynthesis. *Proc Natl Acad Sci U S A* **83**, 9464-9468 (1986).
- 838 43 Feng, Y., Vinogradov, I. & Ge, N. H. General noise suppression scheme with  
839 reference detection in heterodyne nonlinear spectroscopy. *Opt Express* **25**, 26262-  
840 26279 (2017).
- 841 44 Feng, Y., Vinogradov, I. & Ge, N. H. Optimized noise reduction scheme for  
842 heterodyne spectroscopy using array detectors. *Opt Express* **27**, 20323-20346 (2019).
- 843 45 Barty, A. *et al.* Cheetah: software for high-throughput reduction and analysis of serial  
844 femtosecond X-ray diffraction data. *J. Appl. Crystallogr.* **47**, 1118-1131 (2014).
- 845 46 White, T. A. *et al.* CrystFEL: a software suite for snapshot serial crystallography. *J.*  
846 *Appl. Crystallogr.* **45**, 335-341 (2012).
- 847 47 White, T. A. *et al.* Recent developments in CrystFEL. *J. Appl. Crystallogr.* **49**, 680-  
848 689 (2016).
- 849 48 French, S. & Wilson, K. Treatment of Negative Intensity Observations. *Acta*  
850 *Crystallogr A* **34**, 517-525 (1978).
- 851 49 McCoy, A. J. *et al.* Phaser crystallographic software. *J. Appl. Crystallogr.* **40**, 658-674  
852 (2007).
- 853 50 Henderson, R. & Moffat, J. K. The Difference Fourier Technique in Protein  
854 Crystallography: Errors and their Treatment. *Acta Crystallogr. B* **27**, 1414-1420  
855 (1971).
- 856 51 Wickstrand, C., Dods, R., Royant, A. & Neutze, R. Bacteriorhodopsin: Would the real  
857 structural intermediates please stand up? *Biochim Biophys Acta* **1850**, 536-553 (2015).

- 858 52 Brunger, A. T. *et al.* Crystallography & NMR system: A new software suite for  
859 macromolecular structure determination. *Acta Crystallogr D Biol Crystallogr* **54**, 905-  
860 921 (1998).
- 861 53 Ursby, T. & Bourgeois, D. Improved Estimation of Structure-Factor Difference  
862 Amplitudes from Poorly Accurate Data. *Acta Crystallogr. A.* **53**, 564-575 (1997).
- 863 54 Rajagopal, S., Schmidt, M., Anderson, S., Ihee, H. & Moffat, K. Analysis of  
864 experimental time-resolved crystallographic data by singular value decomposition.  
865 *Acta Crystallogr D Biol Crystallogr* **60**, 860-871 (2004).
- 866 55 Schmidt, M., Rajagopal, S., Ren, Z. & Moffat, K. Application of singular value  
867 decomposition to the analysis of time-resolved macromolecular x-ray data. *Biophys J*  
868 **84**, 2112-2129 (2003).
- 869 56 Adams, P. D. *et al.* PHENIX: a comprehensive Python-based system for  
870 macromolecular structure solution. *Acta Crystallogr. D Biol. Crystallogr.* **66**, 213-221  
871 (2010).
- 872 57 Emsley, P. & Cowtan, K. Coot: model-building tools for molecular graphics. *Acta*  
873 *Crystallogr. D Biol. Crystallogr.* **60**, 2126-2132 (2004).
- 874 58 Chen, V. B. *et al.* MolProbity: all-atom structure validation for macromolecular  
875 crystallography. *Acta Crystallogr. D Biol. Crystallogr.* **66**, 12-21 (2010).
- 876 59 Laskowski, R. A., MacArthur, M. W., Moss, D. S. & Thornton, J. M. PROCHECK: a  
877 program to check the stereochemical quality of protein structures. *J. Appl. Cryst.* **26**,  
878 283-291 (1993).
- 879 60 Murshudov, G. N. & Dodson, E. J. Simplified error estimation a la Cruickshank in  
880 macromolecular crystallography. *CCP4 Newsletter on protein crystallography* **33**, 31-  
881 39 (1997).

- 882 61 Grosse-Kunstleve, R. W., Sauter, N. K., Moriarty, N. W. & Adams, P. D. The  
883 Computational Crystallography Toolbox: crystallographic algorithms in a reusable  
884 software framework. *J. Appl. Cryst.* **35**, 126-136 (2002).
- 885 62 Deisenhofer, J., Epp, O., Sinning, I. & Michel, H. Crystallographic refinement at 2.3  
886 Å resolution and refined model of the photosynthetic reaction centre from  
887 *Rhodospseudomonas viridis*. *J. Mol. Biol.* **246**, 429-457 (1995).
- 888 63 Pronk, S. *et al.* GROMACS 4.5: a high-throughput and highly parallel open source  
889 molecular simulation toolkit. *Bioinformatics* **29**, 845-854 (2013).
- 890 64 Duan, Y. *et al.* A point-charge force field for molecular mechanics simulations of  
891 proteins based on condensed-phase quantum mechanical calculations. *J. Comput.*  
892 *Chem.* **24**, 1999-2012 (2003).
- 893 65 Ceccarelli, M., Procacci, P. & Marchi, M. An ab initio force field for the cofactors of  
894 bacterial photosynthesis. *J. Comput. Chem.* **24**, 129-142 (2003).
- 895 66 Ufimtsev, I. S. & Martinez, T. J. Quantum Chemistry on Graphical Processing Units.  
896 3. Analytical Energy Gradients, Geometry Optimization, and First Principles  
897 Molecular Dynamics. *J Chem Theory Comput* **5**, 2619-2628 (2009).
- 898 67 Titov, A. V., Ufimtsev, I. S., Luehr, N. & Martinez, T. J. Generating Efficient  
899 Quantum Chemistry Codes for Novel Architectures. *J Chem Theory Comput* **9**, 213-  
900 221 (2013).
- 901 68 Adamo, C. & Barone, V. Toward Reliable Density Functional Methods without  
902 Adjustable Parameters: The PBE0 Model. *J. Chem. Phys.* **110**, 6158-6170. (1999).
- 903 69 Dunning T.H. & P.J., H. in *Methods of Electronic Structure Theory. Modern*  
904 *Theoretical Chemistry*, Vol. 3 (ed Schaefer H.F.) (Springer, 1977).

905 70 Grimme, S., Antony, J., Ehrlich, S. & Krieg, H. A consistent and accurate ab initio  
906 parametrization of density functional dispersion correction (DFT-D) for the 94  
907 elements H-Pu. *J Chem Phys* **132**, 154104-154101 - 154104-154119 (2010).

908 71 Jorgensen, W. L., Chandrasekhar, J., Madura, J. D., Impey, R. W. & Klein, M. L.  
909 Comparison of simple potential functions for simulating liquid water. *J. Chem. Phys.*  
910 **79**, 926–935 (1983).

911 72 Hirata, S. & Head-Gordon, M. Time-Dependent Density Functional Theory within the  
912 Tamm–Dancoff Approximation. *Chem. Phys. Lett.* **314**, 291-299 (1999).

913 73 Heinis, T., Chowdhury, S., Scott, S. L. & Kebarle, P. Electron Affinities of Benzo-,  
914 Naphtho-, and Anthraquinones Determined from Gas-Phase Equilibria Measurements.  
915 *J. Am. Chem. Soc.* **110**, 400-407 (1988).

916 74 Maiti, S. *et al.* Femtosecond coherent transient infrared spectroscopy of reaction  
917 centers from Rhodobacter sphaeroides. *Proc Natl Acad Sci U S A* **91**, 10360-10364  
918 (1994).

919 75 Pawlowicz, N. P. *et al.* Identification of the first steps in charge separation in bacterial  
920 photosynthetic reaction centers of Rhodobacter sphaeroides by ultrafast mid-infrared  
921 spectroscopy: electron transfer and protein dynamics. *Biophys J* **95**, 1268-1284 (2008).

922  
923  
924  
925  
926

927 **EXTENDED DATA FIGURE LEGENDS**

928

929 **Extended Data Figure 1: Dependence of transient infrared (IR) spectra on the pump**

930 **laser fluence. a,** Time-resolved IR difference spectra recorded from RC<sub>vir</sub> in D<sub>2</sub>O buffer for

931 four time points and variable pump-laser fluence following 960 nm excitation. Spectral

932 changes are consistent with earlier reports.<sup>74,75</sup> Dominant time-dependent features are

933 highlighted and include: (1) a negative band at 1687 cm<sup>-1</sup> (9-carbonyl stretch in SP<sub>L</sub> and SP<sub>M</sub>)

934 and (2) a broad negative band centred at 1680 cm<sup>-1</sup> (9-carbonyl stretch in BCh<sub>L</sub>). Transient

935 changes from  $\Delta t = 2$  ps to 5 ps correlate with the time-dependent photo-oxidation of SP. Grey

936 columns indicate decreasing bands whereas cyan columns indicate increasing bands. **b,** Time

937 resolve IR difference spectra normalized and superimposed. These spectra remain

938 superimposable throughout the pump-laser fluence domain probed. **c,** Dependence of the

939 magnitude of the difference IR signal (calculated as the sum of the absolute value over all

940 pixels) on the pump laser fluence. Below 20 GW/cm<sup>2</sup> the absolute signal increases

941 approximately linearly whereas above 60 GW/cm<sup>2</sup> the signal flattens out as a plateau is

942 reached. This plateau is consistent with the complete bleaching of the special pair absorption

943 at 960 nm in the photoexcited state and correlates with the phenomenon of hole-burning in

944 RC<sub>vir</sub>.<sup>42</sup>

945

946 **Extended Data Figure 2: Overview of the experimental  $F_{\text{obs}}^{\text{light}} - F_{\text{obs}}^{\text{dark}}$  difference**

947 **Fourier electron density maps calculated between the photo-excited and resting state**

948 **data. a,** Overview of the structure of RC<sub>vir</sub> when viewed from the plane of the membrane. TM

949 helices E<sub>L</sub> and D<sub>M</sub> are highlighted in red and gold respectively. **b-h,** Difference Fourier

950 electron density maps for the time-points: **b,**  $\Delta t = 1$  ps; **c,**  $\Delta t = 5$  ps (a); **d,**  $\Delta t = 5$  ps (b); **e,**  $\Delta t$

951  $= 20$  ps; **f,**  $\Delta t = 300$  ps (b); **g,**  $\Delta t = 300$  ps (a); **h,**  $\Delta t = 8$   $\mu$ s. All maps are contoured at  $\pm 4.0 \sigma$

952 ( $\sigma$  is the root mean square electron density of the map). Positive difference electron density is  
953 shown in blue and negative difference electron density is shown in gold.

954

955 **Extended Data Figure 3: Light-induced electron density changes in RC<sub>vir</sub> at the site of**  
956 **photo-oxidation.** Experimental  $F_{\text{obs}}^{\text{light}} - F_{\text{obs}}^{\text{dark}}$  isomorphous difference Fourier electron  
957 density maps for the time-points: **a**,  $\Delta t = 1$  ps. **b**,  $\Delta t = 5$  ps (data set a); **c**,  $\Delta t = 5$  ps (data set  
958 b). **d**,  $\Delta t = 20$  ps; **e**,  $\Delta t = 300$  ps (data set b); **f**,  $\Delta t = 300$  ps (data set a); **g**,  $\Delta t = 8$   $\mu\text{s}$ . **h-i**,  
959 Principal component from SVD analysis of difference Fourier electron density maps for: **h**,  
960 the first four time-points,  $\Delta t = 1$  ps, 5 ps (data set a), 5 ps (data set b) and 20 ps; **i**, the final  
961 three time-points,  $\Delta t = 300$  ps (data set a), 300 ps (data set b) and 8  $\mu\text{s}$ . All maps are  
962 contoured at  $\pm 3.2 \sigma$  (blue, positive difference electron density; gold, negative difference  
963 electron density). Peak heights listed in Table 2 are marked with coloured circles in panels h  
964 and i. **j**, Representation of a sphere of radius 4.5  $\text{\AA}$  used to integrate difference electron  
965 density above a pedestal of 3.0  $\sigma$  as described in reference<sup>20</sup>. Positive difference density  
966 amplitudes (A+) and negative difference density amplitudes (A-) were merged according to  
967  $((A+)^2 + (A-)^2)^{1/2}$  and are displayed in Fig. 2f. These integrated difference electron density  
968 values are also used in the statistical analyses presented in Extended Data Table 2. **k**,  
969 Simulated difference Fourier electron density maps near the SP calculated from the refined  
970 structure for  $\Delta t = 20$  ps versus the refined resting state structure. Data are cut at 2.8  $\text{\AA}$   
971 resolution for comparison with experimental data. The simulated map is contoured at  $\pm 12.0$   
972  $\sigma$ . **l**, Relative magnitude of the singular values resulting from SVD analysis of the difference  
973 Fourier electron density maps for all seven time-points. **m**, First (blue) and second (red)  
974 columns of the unitary matrix U resulting from SVD analysis of all seven time-points  
975 weighted according to their corresponding singular values. The first right singular vector (the  
976 principal SVD component) makes a significant and positive contribution to all time-points. In

977 contrast the difference electron density maps for  $\Delta t = 5$  ps (a) and 300 ps (a) contain strong  
978 negative contributions from the second right singular vector, which suggests that differences  
979 between the two experimental runs cause systematic differences in the difference Fourier  
980 electron density maps that are separated by SVD analysis.

981

982 **Extended Data Figure 4: Electron density changes near the active site of myoglobin.** The

983  $F_{\text{obs}}^{\text{light}} - F_{\text{obs}}^{\text{dark}}$  difference Fourier electron density map for  $\Delta t = 10$  ps was calculated from  
984 data (pdb entries 5CNE minus 5CMV) recorded during TR-SFX studies of the photo-  
985 dissociation of carbon monoxide from the active site of myoglobin.<sup>21</sup> **a**, Data from 15 Å to 1.8  
986 Å were used to calculate the difference Fourier electron density map. **b**, Data from 15 Å to 3.0  
987 Å were used to calculate the difference Fourier electron density map. Positive and negative  
988 difference electron density features associated with the heme group indicate slight motions of  
989 the protoporphyrin-IX. Blue represents positive difference density (contoured at 3.0  $\sigma$ ) and  
990 gold represents negative density (contoured at -3.0  $\sigma$ ). At 1.8 Å the maximum amplitude of  
991 the highlighted difference density features are: a+, 14.5  $\sigma$ ; a-, 14.0  $\sigma$ ; b+, 4.6  $\sigma$ ; b- 4.0  $\sigma$ ; c+,  
992 4.1  $\sigma$ , c- 4.0  $\sigma$ ; d+, 3.8  $\sigma$ . When the map is recalculated after data is cut to 3.0 Å resolution the  
993 corresponding values are: a+, 11.9  $\sigma$ ; a-, 12.4  $\sigma$ ; b+, 4.2  $\sigma$ ; b- 4.1  $\sigma$ ; c+, 3.7  $\sigma$ , c- 2.9  $\sigma$ ; d+, 3.2  
994  $\sigma$ .

995

996 **Extended Data Figure 5: Light-induced electron density changes in RC<sub>vir</sub> within the**

997 **menaquinone binding pocket.** Experimental  $F_{\text{obs}}^{\text{light}} - F_{\text{obs}}^{\text{dark}}$  difference Fourier electron  
998 density maps for the time-points: **a**,  $\Delta t = 1$  ps. **b**,  $\Delta t = 5$  ps (data set a); **c**,  $\Delta t = 5$  ps (data set  
999 b). **d**,  $\Delta t = 20$  ps; **e**,  $\Delta t = 300$  ps (data set b); **f**,  $\Delta t = 300$  ps (data set a); **g**,  $\Delta t = 8$   $\mu$ s. All seven  
1000 maps are contoured at  $\pm 3.0$   $\sigma$  (blue, positive difference electron density; gold, negative  
1001 difference electron density). **h-i**, Principal component from SVD analysis of difference

1002 Fourier electron density maps for: **h**, the first four time-points,  $\Delta t = 1$  ps, 5 ps (data set a), 5 ps  
1003 (data set b) and 20 ps; **i**, the final three time-points,  $\Delta t = 300$  ps (data set a), 300 ps (data set b)  
1004 and 8  $\mu$ s. SVD difference Fourier maps are contoured at  $\pm 3.2 \sigma$ . Peak heights listed in Table  
1005 2 are indicated in panel **i**. **j**, Simulated difference Fourier electron density maps near  $Q_A$   
1006 calculated from the refined structure for  $\Delta t = 300$  ps (data set a) versus the refined resting  
1007 state structure. Data are cut at 2.8 Å resolution for comparison with experimental data. The  
1008 simulated map is contoured at  $\pm 12.0 \sigma$ .

1009

1010 **Extended Data Figure 6: Results of QM/MM energy minimization calculations. a-c**, QM  
1011 subsystems used in the QM/MM optimizations of the co-factors. Atoms included in the QM  
1012 region are shown in ball-and-stick representation, while the other atoms of the protein are  
1013 shown as cartoons. Atoms belonging to the co-factor that are not included in the QM region  
1014 are shown as sticks. Water molecules that are not part of the QM region are not shown. **a**,  
1015 Atoms included in the QM region associated with the SP. **b**, Atoms included in the QM  
1016 region associated with the BPh<sub>L</sub>. **c**, Atoms included in the QM region associated with the Q<sub>A</sub>.  
1017 **d**, Structures of the energy minimized resting conformation (black: SP and BPh<sub>L</sub> neutral) and  
1018 that after the first electron transfer step (blue: SP<sup>+1</sup> and BPh<sub>L</sub><sup>-1</sup>) shown near the special pair. **e**,  
1019 Structures of the energy minimized resting conformation (black: SP and BPh<sub>L</sub> neutral) and  
1020 that after the first electron transfer step (blue: SP<sup>+1</sup> and BPh<sub>L</sub><sup>-1</sup>) shown near BPh<sub>L</sub>. **f**, Structures  
1021 of the energy minimized resting conformation (black: SP and Q<sub>A</sub> neutral) and that after the  
1022 second electron transfer step (blue: SP<sup>+</sup> and Q<sub>A</sub><sup>-</sup>) shown near Q<sub>A</sub>. The H-bond between O<sub>1</sub> of  
1023 the reduced semiquinone and N<sub>δ1</sub> of His217<sub>M</sub> is predicted to be shortened by 0.17 Å when  
1024 menaquinone is reduced. **g-h**, Schematic depiction of the potential energy surfaces for  
1025 menaquinone in vacuum (**g**) and within the protein (**h**) in the resting (neutral) electronic state  
1026 (black) and the reduced electronic state (red). Vertical electron affinities (VEA), adiabatic

1027 electron affinities (AEA) and relaxation energies  $E_r$  were computed at the PBE0-  
1028 D3/LANL2DZ level of DFT for isolated  $Q_A$  and at the PBE0-D3/LANL2DZ/Amber03  
1029 QM/MM level for  $Q_A$  within the protein.

1030

1031 **Extended Data Figure 7: Recurring movements of  $C\alpha$  atoms quantified by structural**  
1032 **refinement.** Recurring movements of  $C\alpha$  atoms quantified by full occupancy structural  
1033 refinement against 100 randomly resampled TR-SFX data sets. Recurring movements are  
1034 represented as error weighted mean ratios relative to 100 control structural refinements  
1035 (Methods). Error weighted means ratios are coloured from grey (< 80 % of the maximum  
1036 ratio) to red ( $\geq 95$  % of the maximum ratio). **a**, Recurring movements of  $C\alpha$  atoms associated  
1037 with refinements against data for  $\Delta t = 1$  ps. **b**, Recurring movements of  $C\alpha$  atoms for  $\Delta t = 5$   
1038 ps (data set a). **c**, Recurring movements of  $C\alpha$  atoms for  $\Delta t = 5$  ps (data set b). **d**, Recurring  
1039 movements of  $C\alpha$  atoms for  $\Delta t = 20$  ps. **e**, Recurring movements of  $C\alpha$  atoms for  $\Delta t = 300$  ps  
1040 (data set b). **f**, Recurring movements of  $C\alpha$  atoms for  $\Delta t = 300$  ps (data set a). **g**, Recurring  
1041 movements of  $C\alpha$  atoms for  $\Delta t = 8 \mu s$ . Transmembrane helices are drawn as rods.

1042

1043

1044 **FOOTNOTES TO EXTENDED DATA TABLES**

1045

1046 **Extended Data Table 1: Crystallographic data and refinement statistics**

1047 Footnotes to Extended Data Table 1

1048 
$$^{\dagger}R_{\text{split}} = 1 / \sqrt{2 \frac{\sum hkl |I_{\text{even}} - I_{\text{odd}}|}{1/2 \sum hkl |I_{\text{even}} + I_{\text{odd}}|}}$$

1049 <sup>‡</sup>Values in parenthesis is those of the highest resolution shell.

1050 <sup>£</sup>Ratio of the number of indexed images to the total number of images.

1051

1052

1053 **Extended Data Table 2: Difference Fourier electron density peak amplitudes**

1054 Footnotes to Extended Data Table 2

1055 \*Positive and negative difference electron density peaks are marked on Extended data Figs.

1056 3h, 3i and 5i. Difference electron density values were read out manually in COOT.

1057 Amplitudes < 2.4  $\sigma$  are not shown.

1058

1059

1060 **Extended Data Table 3: Two sample t-tests of integrated electron density amplitudes**

1061 Footnotes to Extended Data Table 3

1062 \*Mean  $\sigma$ /sphere represents the root-mean-square of the difference electron density above and

1063 below a threshold of  $\pm 3.0 \sigma$  within a sphere of radius 4.5 Å centred on the Mg<sup>2+</sup> atoms of the

1064 BChs; the Fe atoms of the haems; and ring centres of the menaquinone and BPhe cofactors.

1065 All values are scaled relative to a mean value for SP = 1.

1066 <sup>†</sup>The number of elements in each sampled set of the two-sample t-test.

1067 <sup>‡</sup>Difference electron density associated with haem<sub>3</sub> gave the lowest mean  $\sigma$ /sphere (0.14)

1068 and an exceptionally low standard deviation ( $\pm 0.06$ ). Randomly generated control data

1069 gave the corresponding values of  $0.09 \pm 0.22$ . The coincidence of a set with a low standard

1070 deviation being compared against a control set with an exceptionally high standard

1071 deviation frequently yielded low *p*-values. Nevertheless, the experimental difference

1072 features associated with haem<sub>3</sub> are weak and are therefore not physically meaningful.

1073 <sup>£</sup>Thirty two control data sets were generated by randomly selecting a sub-set of the dark

1074 observations to generate a new data set. Sixteen control difference Fourier electron density

1075 maps were then calculated between two of the control data-sets to generate maps

1076 representing the noise inherent within the SFX experiment. Mean  $\sigma$ /sphere calculations and

1077 all other steps proceeded as with the light versus dark experimental difference Fourier

1078 electron density maps.

1079 <sup>£</sup>The reference set consisted of a set of seven maps ( $N_B = 7$ ) randomly selected from

1080 sixteen control maps. Random selection of the control set and the t-test was repeated 1000

1081 times, from a possible set of  $16!/(9! \times 7!) = 11440$  different combinations of the 16 control  
1082 maps. Percentage values give the fraction of occasions when  $p \leq$  threshold for the resulting  
1083 two sample t-test.

1084 <sup>§</sup>The hypothesis that the two sets of the t-test are indistinguishable is either true (0) or false  
1085 (1) at the specified confidence level.

1086 <sup>§</sup> Features identified as distinguishable from noise with a degree of confidence defined by  
1087 the given  $p$ -value.

1088

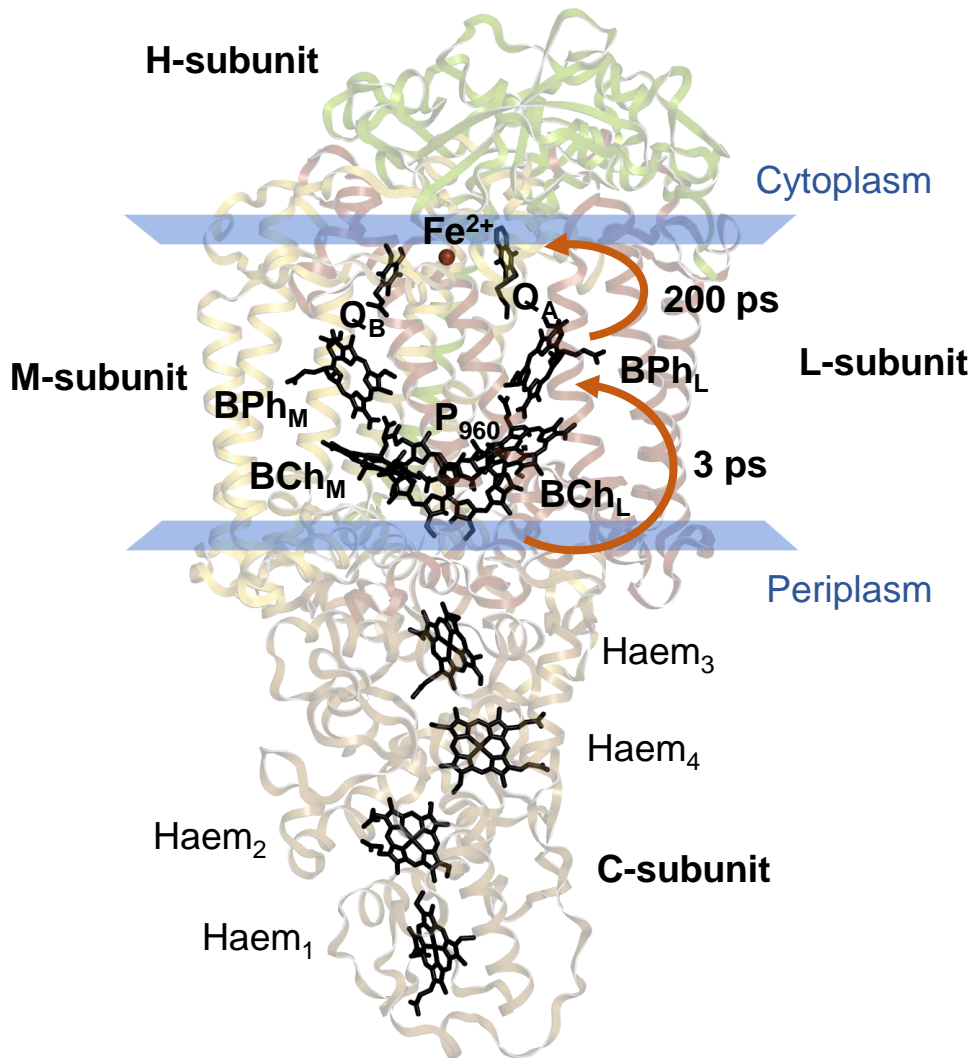


**Figure 1:** Dods et al.

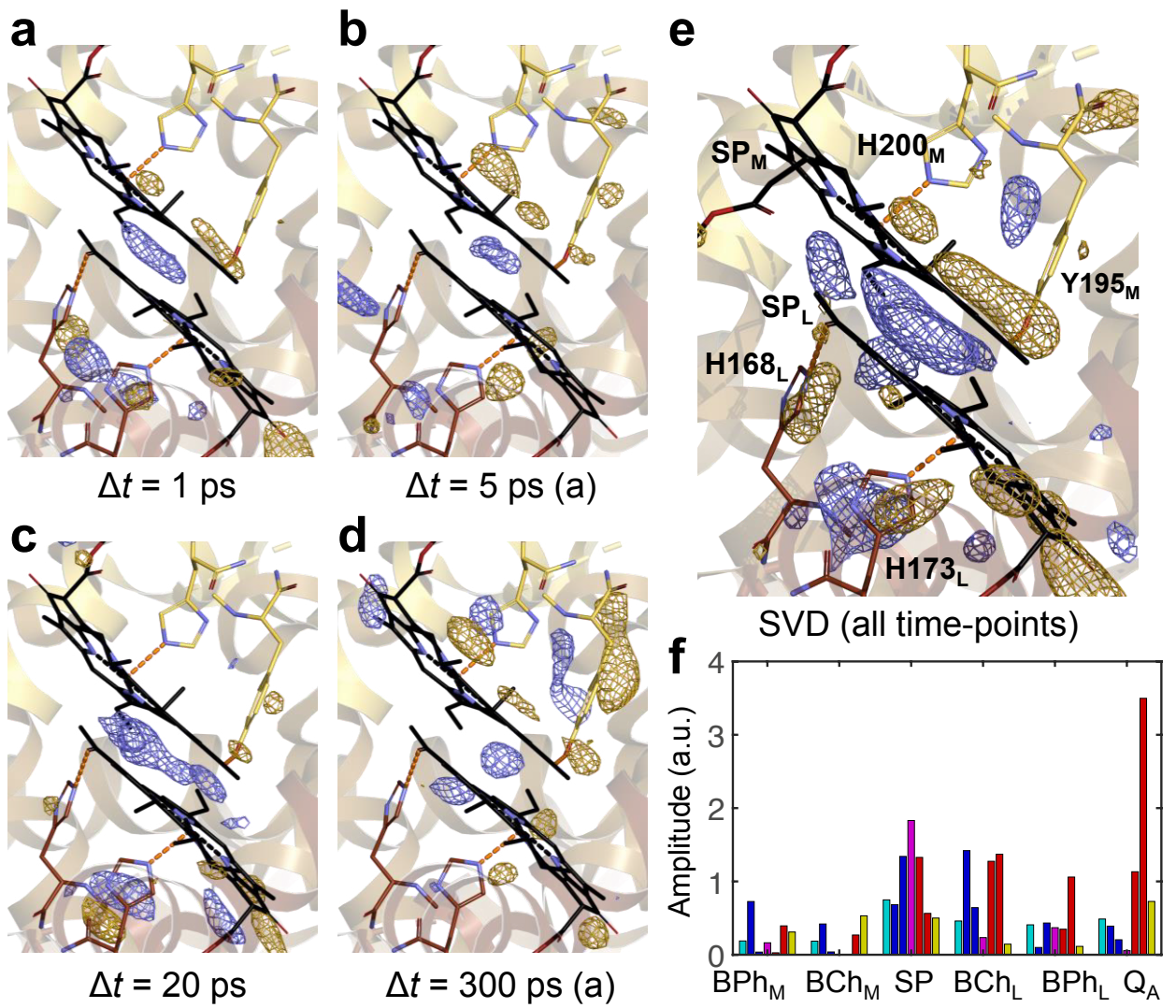


**Figure 2:** Dods et al.

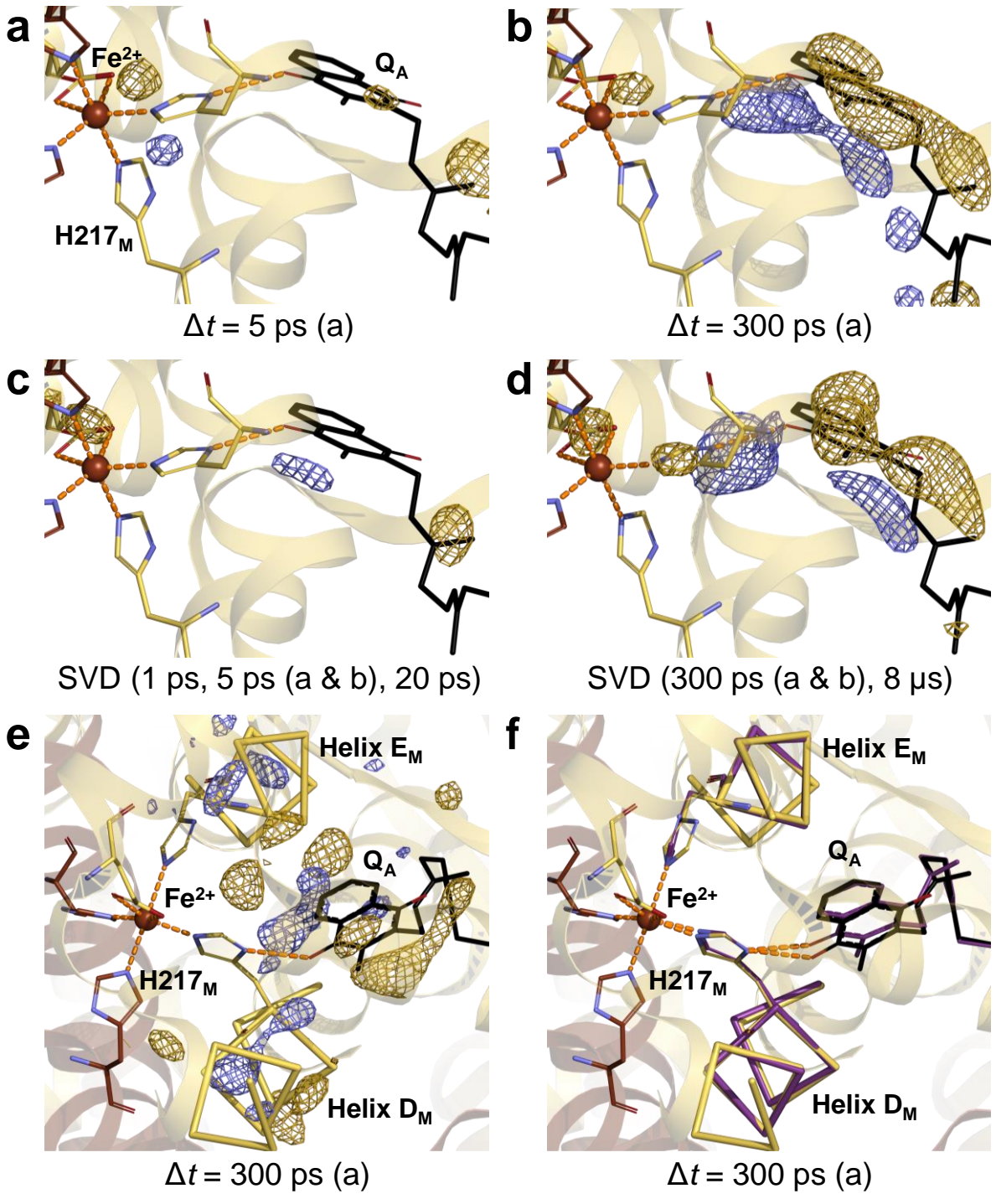


**Figure 3:** Dods et al.

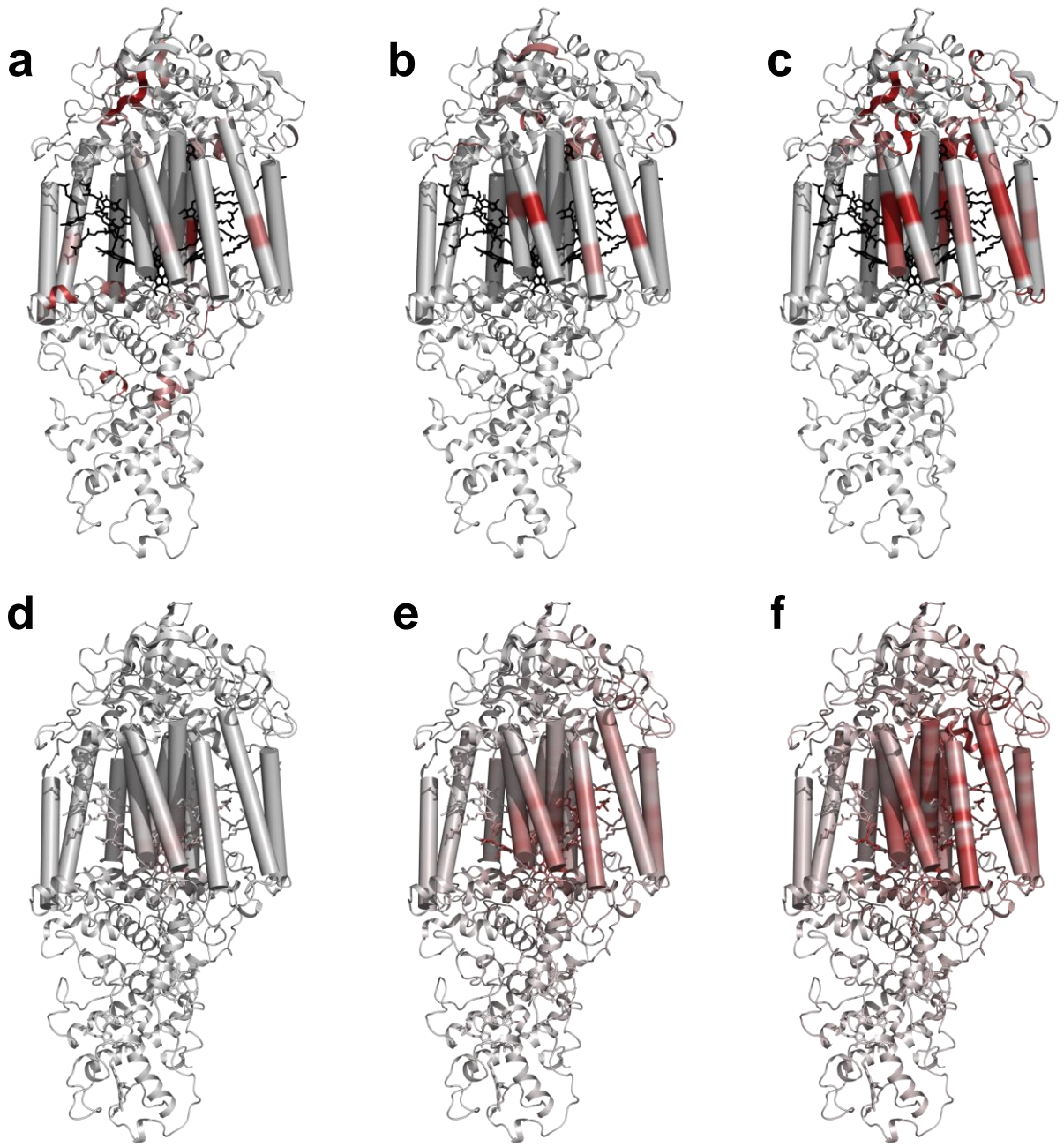


**Figure 4:** Dods et al.